Research Paper

Human-relevant *Ptpn6* mutation alters immune and hepatic functions during aging

Beisy Laborit Labrada[1], Amit Kumar[1,3], Alona Kolnohuz[1], Marie Pineault[1], Kerstin Bellmann[1], Michael Schwab[1], Andréanne Gagné[1] Mathieu Laplante[1,2], Mathieu C Morissette[1,2], André Marette[1,2]

[1]Institut Universitaire de Cardiologie et de Pneumologie de Québec (CRIUCPQ), Université Laval, Québec, QC G1V 4G5, Canada
[2]Department of Medicine, Université Laval, Quebec, QC G1V 0A6, Canada
[3]Princess Margaret Cancer Centre, University Health Network, Toronto, ON M5G 2C4, Canada

Correspondence to: André Marette; **email:** andre.marette@criucpq.ulaval.ca
Keywords: SHP-1/Ptpn6, B cell, macrophage, aging, *Ptpn6*^{Ala457Thr}
Received: December 1, 2025 **Accepted:** July 27, 2026 **Published:** August 28, 2026

ABSTRACT

Src homology region 2-containing phosphatase 1 (SHP-1), encoded by the protein tyrosine phosphatase non-receptor type 6 (*PTPN6*), regulates immune and metabolic signaling pathways. Although its functions in immune cells and insulin-responsive tissues are separately established, its integrative function in immunometabolic regulation remains unclear. A damaging variant in the *PTPN6* gene (Ala455Thr) was discovered in a French-Canadian family and found to be the cause of early-onset emphysema. Using mice carrying this whole-body human-relevant mutation, we studied immunometabolic phenotypes across aging. Old mutant mice showed decreased body, liver and adipose tissue weights, improved glucose tolerance, and enhanced hepatic insulin sensitivity. Despite improved metabolic parameters, aged mutant mice developed liver abnormalities, including increased fibrosis and aberrant immune cell infiltration. Transcriptomic and histological analyses revealed an age-associated accumulation of intrahepatic B lymphocytes and macrophages, accompanied by increased SHP-1 protein levels and activation of Signal transducer and activator of transcription 3 (STAT3) signaling. Experiments in primary hepatocytes and old hepatocyte-specific *Ptpn6* knockout mice suggest that these alterations are driven by immune rather than intrinsic hepatocyte mechanisms. These findings identify SHP-1 as a critical modulator of liver immune homeostasis during aging and demonstrate that immune cell infiltration contributes to age-related hepatic remodeling under SHP-1 deficiency.

INTRODUCTION

Src homology region 2-containing phosphatase 1 (SHP-1), encoded by the *PTPN6* gene, is a protein tyrosine phosphatase that plays a crucial role in regulating multiple signaling pathways. The *PTPN6* gene encodes two major forms of SHP-1 protein due to tissue-specific promoters. One form is expressed mostly in epithelial cells, whereas a slightly shorter isoform is almost exclusively expressed in hematopoietic cells [1, 2]. The two proteins differ in the N-terminal amino acids, but their phosphatase activity remains similar [3, 4].

Hematopoietic SHP-1 functions as a negative regulator of both innate and adaptive immune responses [5, 6]. Its role in myeloid cells has been extensively characterized, where it is recruited to immunoreceptor tyrosine-based inhibition motif (ITIM)-containing receptors such as the paired immunoglobulin-like receptor B (PIR-B) [7] and the signal regulatory protein alpha (SIRPα) [8] to limit

activating signals from immunoreceptor tyrosine-based activation motif (ITAM)-containing proteins such as integrins [9], and immunoglobulin Fc receptors (FcRs) [10]. It also modulates cytokine and growth factor signaling by dephosphorylating Janus kinases (JAKs) and Signal transducer and activator of transcription (STAT) proteins [11, 12] downstream of receptors including colony-stimulating factor 1 (CSF1R) and c-Kit receptors [13–15]. In lymphoid cells, SHP-1 similarly limits activation of the T cell receptor (TCR) by targeting lymphocyte specific protein tyrosine kinase (Lck) [16] and zeta-chain of T cell receptor associated protein kinase 70 (ZAP-70) [17, 18] as well as adaptor proteins like linker for activation of T cells (LAT) [19] together with SH2-domain-containing leukocyte protein of 76 kDa (SLP-76) [20]. In contrast, SHP-1's role in B lymphocytes is not as well defined, although it attenuates B cell receptor (BCR) signaling after being recruited to inhibitory co-receptors such as the cluster of differentiation 22 (CD22), cluster of differentiation 72 (CD72), PIR-B, and the Fc gamma receptor IIB (FcγRIIB) [21].

Beyond its immune functions, SHP-1 is also expressed in metabolic tissues, where it is a critical negative regulator of insulin signaling [22–25]. In the liver, SHP-1 negatively regulates insulin clearance by dephosphorylating the transmembrane glycoprotein carcinoembryonic antigen-related cell adhesion molecule-1 (CEACAM1) [26]. We demonstrated that hepatocyte-specific SHP-1 knockout mice fed a high-fat diet (HFD) exhibit improved fasting glucose levels and reduced insulin resistance compared to HFD-fed wildtype mice [24, 27]. Although liver specific SHP-1 knockout mice are more susceptible to hepatic steatosis under HFD conditions, they exhibit lower levels of hepatic inflammation, as indicated by reduced levels of pro-inflammatory cytokines and chemokines such as interleukin 3 (IL-3), interleukin 6 (IL-6), regulated upon activation normal T cell expressed and secreted (RANTES) and tumor necrosis factor (TNFα) compared to wildtype controls [27].

Alterations in immune function and metabolic homeostasis are part of the widespread physiological changes taking place during aging. The immune system undergoes impaired innate and adaptive immune responses, chronic low-grade inflammation, and dysregulated leukocyte signaling [28, 29]. Concomitantly, metabolic tissues exhibit reduced insulin sensitivity and increased lipid accumulation, contributing to the development of age-related conditions such as type 2 diabetes and metabolic-associated steatotic liver disease (MASLD) [30–32]. SHP-1's dual role in immune and metabolic regulation places this tyrosine phosphatase at a critical regulatory node in liver homeostasis in health and disease.

Many *in vivo* functions of SHP-1 have been discovered using the classical motheaten (*Ptpn6*$^{me\text{-}v/me\text{-}v}$) mouse model [33], which carries a whole-body dysfunctional SHP-1 protein. Although this model has been instrumental in revealing the importance of SHP-1 in immune regulation and inflammation, its severe systemic phenotype and early lethality limit the study of SHP-1 function over time. To overcome these limitations, we use a viable genetic mouse model carrying the human-relevant *Ptpn6*^{Ala457Thr} mutation to investigate the effects of SHP-1 dysfunction across life. The corresponding human mutation, *PTPN6*^{Ala455Thr}, was first identified in a French-Canadian family as the cause of early-onset and severe emphysema. In humans, this autosomal dominant heterozygous mutation results in a moderate reduction of SHP-1 phosphatase activity [34]. Unlike motheaten mice, *Ala457Thr* mutants' lifespan is similar to their wildtype counterparts, providing a unique opportunity to study the long-term metabolic and inflammatory impacts of partial SHP-1 dysfunction. While the Ala455Thr variant is known to cause emphysema in humans, it remains unclear whether alterations also occur in metabolic organs such as the liver, as observed in motheaten and hepatocyte-specific SHP-1 knockout mouse models [24, 26, 27]. In addition, the late-onset nature of the disease raises the question of whether other tissues such as the liver would also be affected with aging.

Our findings demonstrate that chronic SHP-1 dysfunction is associated with aberrant intrahepatic accumulation of B cells and macrophages as well as liver fibrosis in aged *Ptpn6*^{Ala457Thr} mice. Despite these liver abnormalities, *Ptpn6*^{Ala457Thr} mice exhibit increased liver insulin sensitivity and improved glucose tolerance during aging. The immunometabolic phenotypes of aged mice bearing the *Ptpn6*^{Ala457Thr} mutation are not detected in young adult mice where B cell and macrophage infiltration is not yet observed. This study identifies SHP-1 as a key modulator of age-associated liver remodeling, whereby partial but chronic loss of SHP-1 function is associated with a previously unrecognized link between immune cell dynamics, hepatic insulin sensitivity and glycemic control during aging.

RESULTS

Ptpn6^{Ala457Thr} phenotypes manifest later in life

To study the immunometabolic and hepatic effects of the human-relevant *Ptpn6*^{Ala457Thr} mutation during the life cycle, chow-fed wildtype (WT) and heterozygous

Ptpn6^{Ala457Thr} mutant male mice were studied at 5.6 (young adult) or 16-19 (old) months of age (Figure 1A). To determine the impact of the *Ptpn6*^{Ala457Thr} mutation on SHP-1 activity *in vivo*, we assessed the tyrosine phosphorylation of CEACAM1, a well-known substrate of SHP-1 [26], immunoprecipitated from liver lysates of young adult and old WT or mutant mice. CEACAM1 tyrosine phosphorylation was increased in the liver of young adult and old mutant mice indicating that SHP-1 phosphatase activity is reduced throughout life in the *Ptpn6*^{Ala457Thr} heterozygous mutants (Supplementary Figure 1A–1D).

We assessed the body and tissue weights of young adult and old WT and *Ptpn6*^{Ala457Thr} mice. Interestingly, reduced body weights were exclusively observed in old *Ptpn6*^{Ala457Thr} mice compared to old WT littermates, while no differences were detected between the young adult groups (Figure 1B). Concomitant with these findings, liver, adipose tissues (mesenteric and brown adipose tissue), as well as kidney and soleus weights were decreased in old, but not young adult *Ptpn6*^{Ala457Thr} mice (Figure 1C–1G). Gastrocnemius muscle and inguinal white adipose tissue weights were not changed either in young adult, or old mice (Figure 1H, 1I). Importantly, the reduction of adipose tissues (mesenteric and brown adipose tissues) remained significant after normalization to body weight (Supplementary Table 1) indicating an organ-specific effect beyond the general reduction in body mass in old *Ptpn6*^{Ala457Thr} mice. In contrast, reduction in liver and kidney weights were proportional to the body weight loss (Supplementary Table 1). Similarly to previously described SHP-1 mutants (*Ptpn6*$^{me\text{-}v/me\text{-}v}$, *Ptpn6*$^{me\text{-}B2/me\text{-}B2}$ and *Ptpn6*$^{m1Btlr/m1Btlr}$) [33, 35, 36] we observed that the *Ptpn6*^{Ala457Thr} mutation causes splenomegaly, but this was only observed in old mice (Figure 1J). These data indicate that the *Ptpn6*^{Ala457Thr} phenotype manifests later in life. Importantly, food intake was comparable between WT and *Ptpn6*^{Ala457Thr} mice in both young adult and old groups (Figure 1K), thereby excluding reduced food intake as a confounding factor underlying the observed differences in organ and tissue weights.

Ptpn6^{Ala457Thr} genotype improves glucoregulation and liver insulin action in aging

Considering that SHP-1 is a well-known regulator of glucose metabolism and insulin signaling [24, 26, 27] we investigated the modulation of glucose metabolism in *Ptpn6*^{Ala457Thr} mutant mice. Compared to WT littermates, the *Ptpn6*^{Ala457Thr} young adult mice displayed comparable fasting blood glucose and insulin levels (Figure 2A, 2B). Similarly, glucose tolerance and insulin stimulated hepatic Akt phosphorylation remained unchanged between genotypes (Figure 2C–2H). In contrast, old *Ptpn6*^{Ala457Thr} mice were more glucose tolerant and insulin sensitive than their old WT littermates, as they displayed lower fasting glycaemia, smaller glucose excursion curves, and enhanced hepatic insulin stimulated Akt phosphorylation on Thr308 (Figure 3A–3H). The levels of insulin stimulated Akt phosphorylation in other insulin sensitive tissues such as mesenteric white adipose tissue (Supplementary Figure 2A, 2B) and gastrocnemius (Supplementary Figure 2C, 2D) remained unchanged in the old *Ptpn6*^{Ala457Thr} mutants. Together, these results show that the *Ptpn6*^{Ala457Thr} phenotype needs time to develop, and that glucose homeostasis in the old *Ptpn6*^{Ala457Thr} mice is positively modulated due to enhanced hepatic insulin signaling, which points to the liver as a key metabolic organ affected by this SHP-1 mutation during aging.

Immune cell infiltration and fibrosis in liver of old *Ptpn6*^{Ala457Thr} mice

To further characterize the liver phenotype of *Ptpn6*^{Ala457Thr} mice, we measured hepatic lipid content and performed histopathological analysis. Fasting plasma and liver triglycerides were unchanged between young adult wildtype and *Ptpn6*^{Ala457Thr} littermates (Figure 4A, 4B). However, triglyceride levels were decreased both in plasma and liver of old *Ptpn6*^{Ala457Thr} mice (Figure 4C, 4D). H&E and Picrosirius red staining revealed an abnormal accumulation of intrahepatic immune cells together with an exacerbated build-up of collagen in the livers of old *Ptpn6*^{Ala457Thr} mice compared with their WT littermates, while such differences were not observed between young adult WT and mutant mice. The histological scoring for total steatosis was lower in the young adult and old *Ptpn6*^{Ala457Thr} mice compared to WT mice (Figure 4E–4H). Overall, these findings support the concept that chronic reduction of SHP-1 phosphatase activity is associated with a late-onset remodeling of the liver, characterized by immune cell accumulation, increased collagen deposition, and reduced lipid accretion, while preserving hepatic insulin sensitivity.

We next performed RNA sequencing using whole livers of old WT and *Ptpn6*^{Ala457Thr} mice to further investigate the molecular mechanisms underlying these genotypic differences. We found 1243 differentially expressed genes between WT and mutant mice. While 959 genes were upregulated, only 284 were downregulated in the *Ptpn6*^{Ala457Thr} mice. As expected from histological analysis, most of the upregulated genes like *Pirb* (log_2FC = 1.82, padj = 3.34e-20), *Itgal* (log_2FC = 1.65, padj = 1.91e-18), *Cd5l* (log_2FC = 1.78, padj = 1.91e-18), *Pou2f2* (log_2FC = 2.03, padj = 3.12e-15), *Adgre1* (log_2FC = 1.57, padj = 4.31e-15) (Figure 5A) were immune cell-specific in accordance with the observed

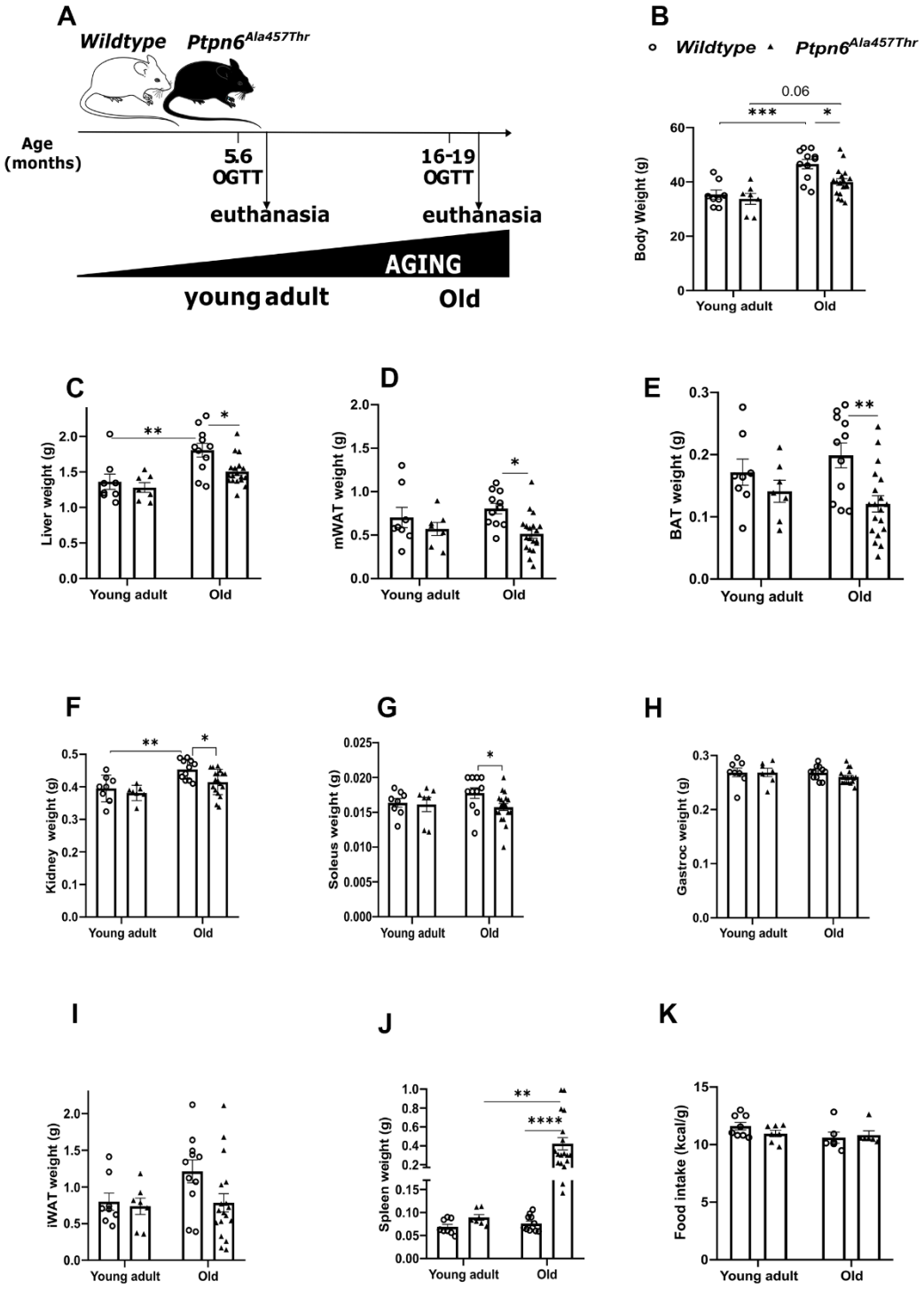

Figure 1. Age- and genotype-dependent changes in body and organ weights in wildtype and *Ptpn6*^{Ala457Thr} mice. (**A**) Experimental timeline showing the design of the animal study comparing wildtype and *Ptpn6*^{Ala457Thr} C57BL/6N mice at 5.6 months (young adult) and 16-19 months (old) of age. Image created with Servier Medical Art (https://smart.servier.com/), licensed under CC BY 4.0 (https://creativecommons.org/licenses/by/4.0/). (**B**) Body weights of young adult and old wildtype and *Ptpn6*^{Ala457Thr} mice. (**C**–**J**) Weights of various adipose tissues and organs: (**C**) liver, (**D**) mesenteric white adipose tissue (mWAT), (**E**) brown adipose tissue (BAT), (**F**) kidney, (**G**) soleus muscle, (**H**) gastrocnemius muscle (Gastroc), (**I**) inguinal white adipose tissue (iWAT), and (**J**) spleen. (**K**) Food intake measured in young adult and old wildtype and *Ptpn6*^{Ala457Thr} mice. Each dot represents an individual animal. Data are presented as mean ± SEM. Statistical significance was assessed using two-way Anova followed by Tukey's post hoc test, with *p < 0.05, **p < 0.01, ***p < 0.001. Sample sizes: Young adult wildtype, n =8; *Ptpn6*^{Ala457Thr}, n = 7 and old wildtype, n = 11; *Ptpn6*^{Ala457Thr}, n=18. Sample sizes for panel (**K**): young adult wildtype, n = 8; *Ptpn6*^{Ala457Thr}, n = 7; old wildtype, n = 6; *Ptpn6*^{Ala457Thr}, n = 6.

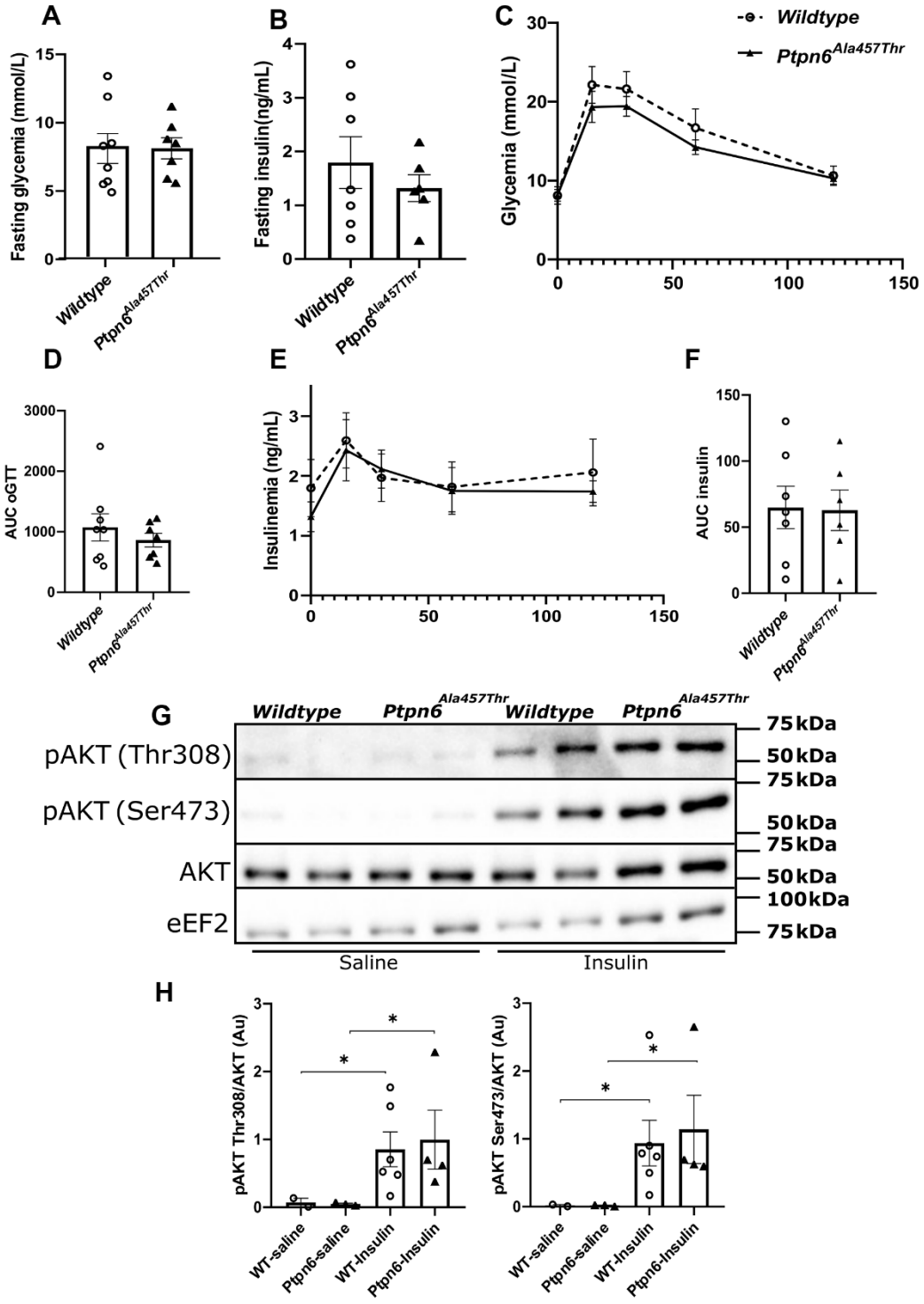

Figure 2. Similar metabolic phenotype in the young adult wildtype and *Ptpn6*^{Ala457Thr} mice. (**A**) Fasting blood glucose and plasma insulin levels (**B**) of young adult wildtype and *Ptpn6*^{Ala457Thr} mice. (**C**) Oral glucose tolerance test (OGTT), glucose levels were measured at the indicated time points following oral glucose administration. (**D**) Area under the curve (AUC) of the glucose response from the OGTT shown in panel (**C**). (**E**) Plasma insulin levels during the OGTT in wildtype and *Ptpn6*^{Ala457Thr} mice. (**F**) AUC of the insulin secretion. (**G**) Western blot analysis of hepatic AKT phosphorylation in young adult mice. (**H**) Quantification of phospho-AKT (Thr308) and phospho-AKT (Ser473) levels normalized to total AKT. Data are presented as mean ± SEM. Statistical analyses were performed using a two-way ANOVA or a mixed-effects model for repeated measures, followed by Tukey's post hoc multiple comparisons test or an unpaired two-tailed Student's t-test, as appropriate. Statistical significance was defined as *p < 0.05, **p < 0.01, ***p < 0.001. Sample sizes: wildtype, n = 7-8; *Ptpn6*^{Ala457Thr}, n = 6-7 Au, arbitrary units.

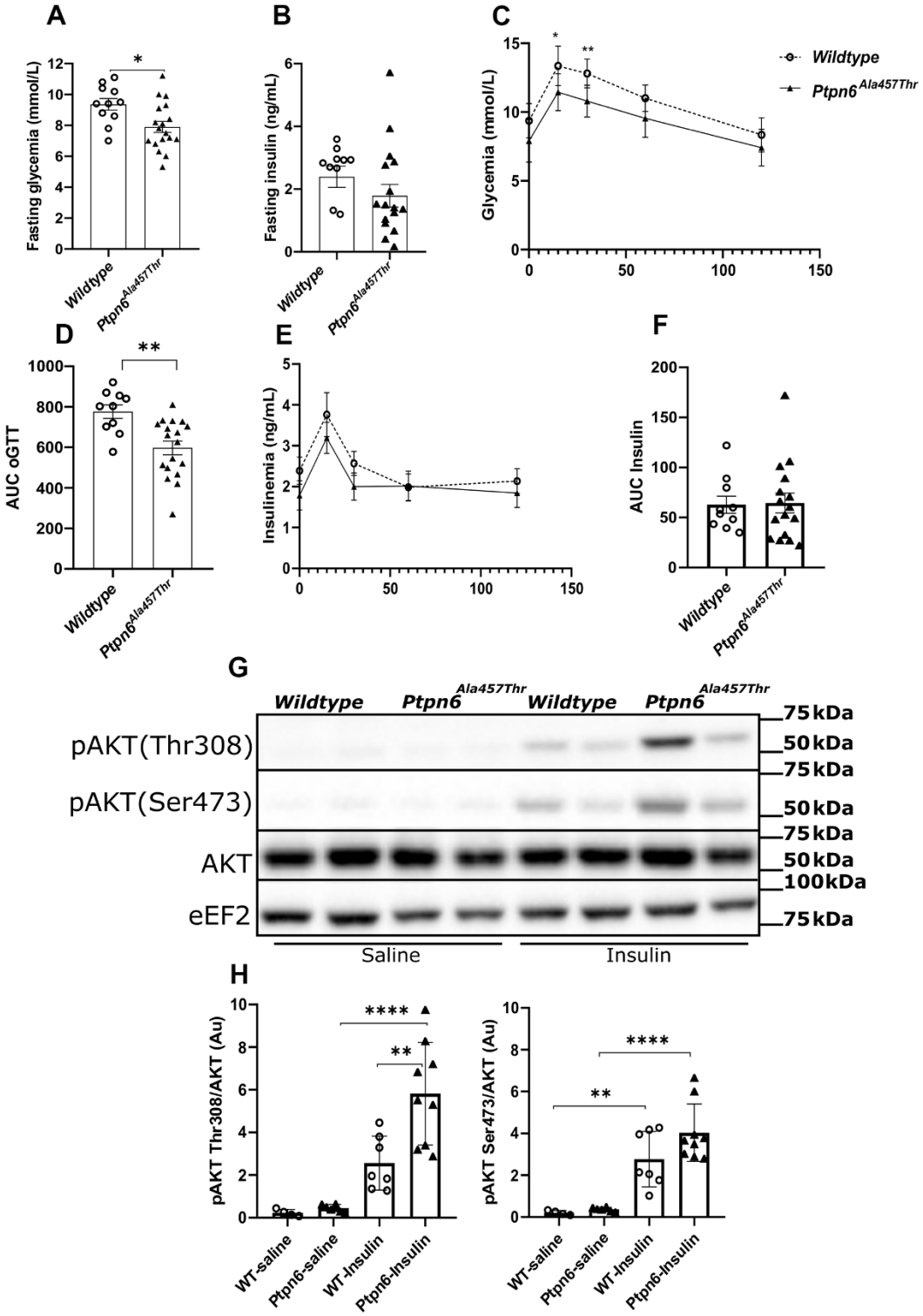

Figure 3. The *Ptpn6*^{Ala457Thr} mutation modulates glucose tolerance during aging. (**A**) Fasting blood glucose and plasma insulin levels (**B**) of old wildtype and *Ptpn6*^{Ala457Thr} mice. (**C**) Oral glucose tolerance test (OGTT), glucose levels were measured at the indicated time points following oral glucose administration. (**D**) Area under the curve (AUC) of the glucose response from the OGTT shown in panel c. (**E**) Plasma insulin levels during the OGTT in wildtype and *Ptpn6*^{Ala457Thr} mice. (**F**) AUC of insulin secretion. (**G**) Western blot analysis of hepatic AKT phosphorylation in old mice. (**H**) Quantification of phospho-AKT (Thr308) and phospho-AKT (Ser473) levels normalized to total AKT. Data are presented as mean ± SEM. Statistical analyses were performed using a two-way ANOVA or a mixed-effects model for repeated measures, followed by Tukey's post hoc multiple comparisons test or an unpaired two-tailed Student's t-test, as appropriate. Statistical significance was defined as *p < 0.05, **p < 0.01, ***p < 0.001. Sample sizes: wildtype, n=10-11; *Ptpn6*^{Ala457Thr}, n = 16-18. Au, arbitrary units.

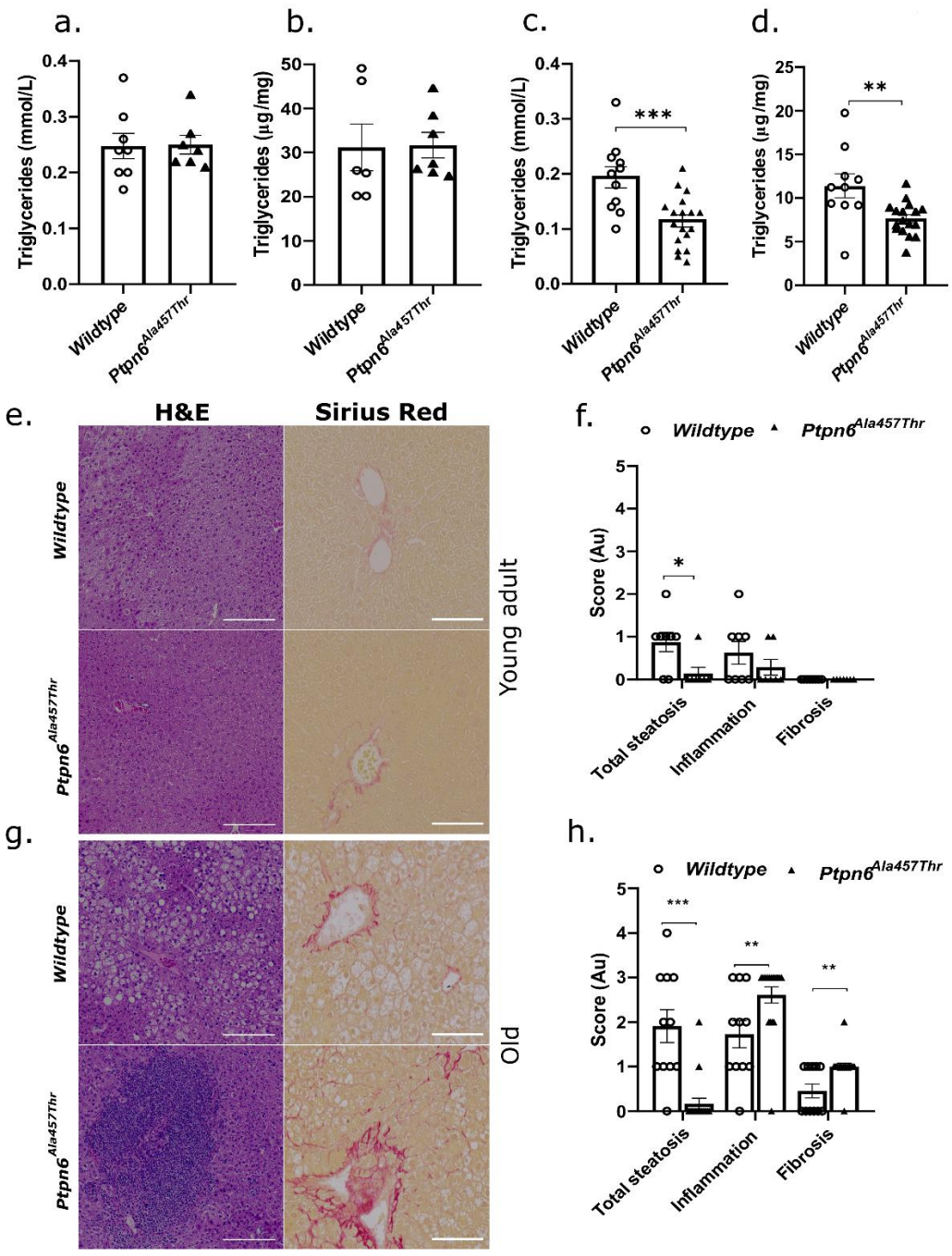

Figure 4. *Ptpn6*^{Ala457Thr} old mice develop liver injury. (**A**) Plasma triglyceride levels in young adult wildtype and *Ptpn6*^{Ala457Thr} mice. (**B**) Hepatic triglyceride content measured from liver extracts in young adult wildtype and *Ptpn6*^{Ala457Thr} mice. (**C**) Plasma triglyceride levels in old wildtype and *Ptpn6*^{Ala457Thr} mice. (**D**) Hepatic triglyceride content measured from liver extracts in old wildtype and *Ptpn6*^{Ala457Thr} mice. (**E**) Representative liver sections from young adult wildtype and *Ptpn6*^{Ala457Thr} mice stained with hematoxylin and eosin (H&E) to assess general histology, and Picrosirius Red to evaluate collagen deposition and fibrosis. Scale bar: 100 µm. (**F**) Histological scoring of total steatosis, inflammation, and fibrosis, based on blinded pathological assessment of liver sections from young adult wildtype and *Ptpn6*^{Ala457Thr} mice. (**G**) Representative liver sections from old wildtype and *Ptpn6*^{Ala457Thr} mice stained with H&E and Picrosirius Red. (**H**) Histological scoring of total steatosis, inflammation, and fibrosis, based on blinded pathological assessment of liver sections from old wildtype and *Ptpn6*^{Ala457Thr} mice. Data are presented as mean ± SEM. Statistical analysis was performed using an unpaired two-tailed Student's t-test, with *$p < 0.05$, **$p < 0.01$, ***$p < 0.001$. Sample sizes: young adult WT, n = 6-8; *Ptpn6*^{Ala457Thr}, n = 7, old WT, n=10-11; *Ptpn6*^{Ala457Thr}, n=17-18.

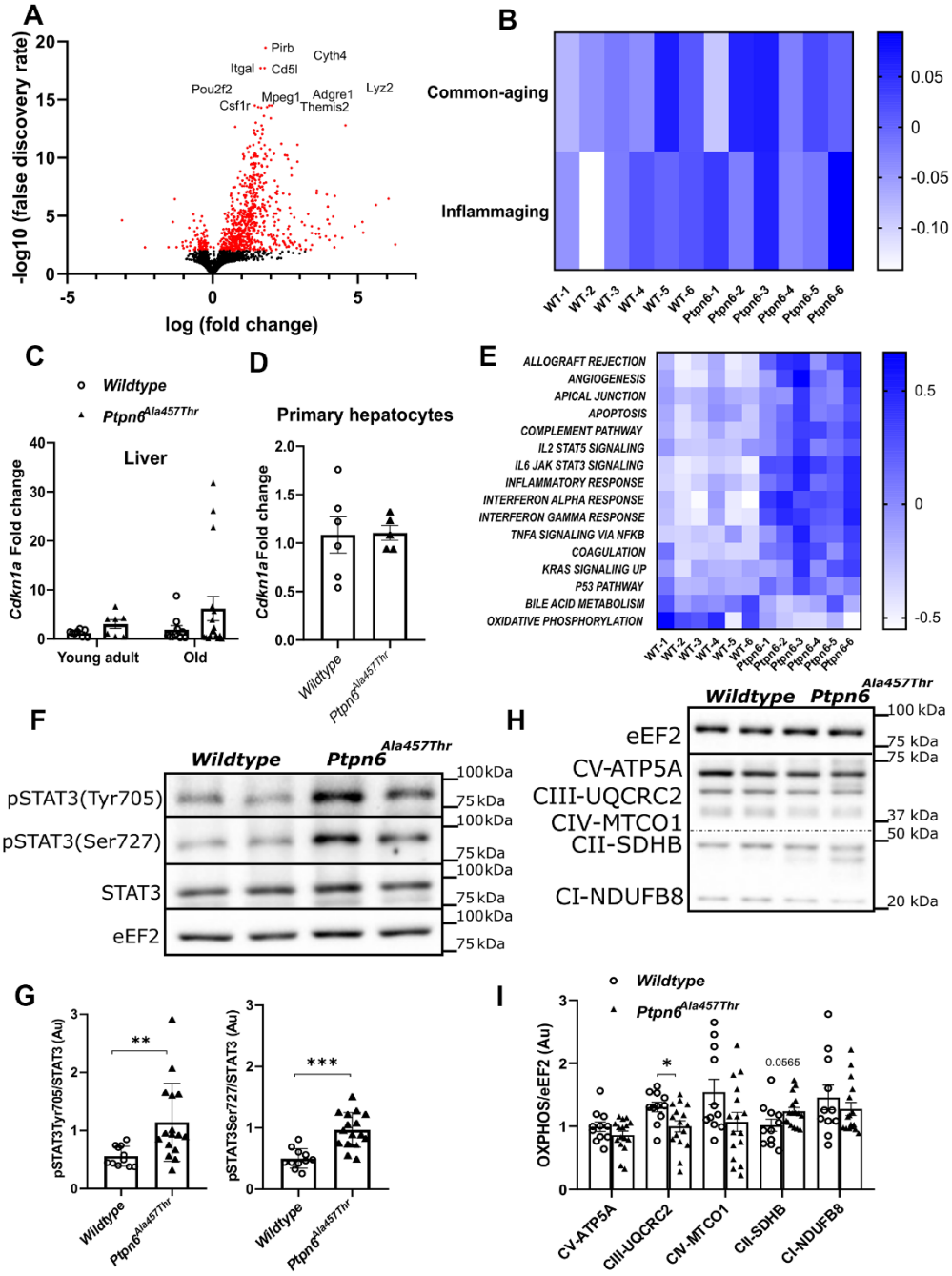

Figure 5. Transcriptomic and immunometabolic alterations in the livers of old mutant mice. (**A**) Volcano plot showing differentially expressed genes in liver RNA-seq data from old wildtype and *Ptpn6*^{Ala457Thr} mice (n = 6 per group). Differential expression analysis was performed using DESeq2, with significance thresholds set at adjusted p<0.05 and $\log_2$ fold change >1. (**B**) Gene signature analysis of common-aging and inflammaging pathways in liver RNA-seq data from old WT and *Ptpn6*^{Ala457Thr} mice. Expression values were scaled per gene (z-score). (**C**) Gene expression levels of *Cdkn1a* in the livers of young adult and old mice and (**D**) primary mouse hepatocytes from old mice. (**E**) Pathway enrichment analysis using the Hallmark gene set database (MSigDB), showing significantly upregulated and downregulated pathways in *Ptpn6*^{Ala457Thr} versus wildtype livers. (**F**) Representative western blot analysis of phosphorylated STAT3 (Tyr705), phosphorylated STAT3 (Ser727) and total STAT3 in liver lysates from old wildtype and *Ptpn6*^{Ala457Thr} mice. (**G**) Quantifications of phosphorylated STAT3 (Tyr705) and phosphorylated STAT3 (Ser727) from panel f. (**H**) Representative western blot showing expression of oxidative phosphorylation complex proteins (OXPHOS) (Complexes I–V) in liver lysates from old wildtype and *Ptpn6*^{Ala457Thr} mice. (**I**) Quantification of OXPHOS from (**H**). Data are presented as mean ± SEM. Statistical significance was assessed using two-way ANOVA or a mixed-effects model for repeated measures, followed by Tukey's post hoc multiple comparisons test or an unpaired two-tailed Student's t-test, as appropriate. Statistical significance was defined as *p < 0.05, **p < 0.01, ***p < 0.001. Sample sizes: old WT, n=10-11; *Ptpn6*^{Ala457Thr}, n=16-17; young adult WT, n=8 and *Ptpn6*^{Ala457Thr}, n=7; Primary mouse hepatocytes WT, n=6 and *Ptpn6*^{Ala457Thr}, n=5. Au, arbitrary units.

immune cell infiltration in the livers of old *Ptpn6*^{Ala457Thr} mice (Figure 4G, 4H). Notably, when applying published common-aging and inflammaging gene signatures derived from a genome-wide CRISPRi screen [37], no differences were detected between aged WT and *Ptpn6*^{Ala457Thr} livers (Figure 5B), suggesting that the transcriptional changes observed in *Ptpn6*^{Ala457Thr} mice are not driven by a generalized acceleration of liver aging. Concomitantly, hepatic expression of the senescence marker *Cdkn1a* did not differ between wildtype and mutant mice in either young adult or aged groups, and this was also observed in primary hepatocytes isolated from aged mice (Figure 5C, 5D). Gene set enrichment analysis (GSEA) revealed that several immune-related pathways were upregulated in the liver of *Ptpn6*^{Ala457Thr} mutants including the IL6-JAK-STAT3-pathway (Figure 5E). By negatively regulating STAT3, SHP-1 has been implicated in the modulation of fibrosis during the development of hepatocellular carcinoma [38, 39], which is consistent with the increased collagen deposition we observed in the liver of old *Ptpn6*^{Ala457Thr} mice (Figure 4G, 4H). Therefore, we performed immunoblot analysis to evaluate the phosphorylation levels of the two STAT3 activation sites, Tyr705 and Ser727. In the livers from old *Ptpn6*^{Ala457Thr} mice, STAT3 phosphorylation of both sites increased compared to their wildtype littermates (Figure 5F, 5G). These results suggest that one of the mechanisms by which this mutation affects the liver might be through the SHP-1-STAT3 axis, but in a context of immune dysregulation. The predominance of altered immune function in old *Ptpn6*^{Ala457Thr} mutants is supported by the finding that the livers of these mice were also characterized by elevated expression of SHP-1 as compared to WT littermates (Supplementary Figure 3A, 3B). Specifically, the hematopoietic transcript of isoform a of *Ptpn6* was increased in livers of old mutant mice, while the non-hematopoietic/epithelial transcript of isoform b was actually reduced in these livers (Supplementary Figure 3C, 3D).

Interestingly, many of the downregulated genes were related to mitochondrial function. Concomitant with this, one of the few downregulated pathways was oxidative phosphorylation (Figure 5E). To validate this, we quantified the protein levels of OXPHOS enzymes and found that complex III ubiquinol-cytochrome c reductase was reduced in the liver of *Ptpn6*^{Ala457Thr} mice compared to their wildtype littermates (Figure 5H, 5I). Overall, these findings suggest that the abnormal infiltration of immune cells in the old *Ptpn6*^{Ala457Thr} mutant mice might impact key processes such as cellular respiration and collagen deposition.

To determine whether the observed STAT3 phenotype originated from regulation within hepatocytes or if it was the result of immune cell infiltration in the liver, we isolated primary mouse hepatocytes from old wildtype and *Ptpn6*^{Ala457Thr} mice. Analysis of STAT3 phosphorylation in primary hepatocytes did not show any difference between the genotypes (Supplementary Figure 4A, 4B). Also, protein levels of OXPHOS enzyme complexes remained unchanged between hepatocytes from old wildtype and *Ptpn6*^{Ala457Thr} littermates and these cells displayed similar oxygen consumption rates (OCR) (Supplementary Figure 4C–4E). Altogether, these results suggest that the hepatic phenotype of the *Ptpn6*^{Ala457Thr} mutation is primarily associated with alterations in infiltrating immune cells, rather than intrinsic changes in hepatocytes.

Ptpn6^{Ala457Thr} mutation causes aberrant hepatic infiltration of B cells and macrophages during aging

To further analyze which immune cell populations are enriched in the liver of old *Ptpn6*^{Ala457Thr} mice, we used a microenvironment cell populations-counter (MCP-counter) method, as previously described [40, 41]. We identified B cells and macrophages as the two populations of immune cells greatly upregulated in the liver of *Ptpn6*^{Ala457Thr} mice during aging (Figure 6A). To refine these observations, we performed complementary immune deconvolution using the xCell algorithm as previously described [41, 42]. This analysis confirmed the enrichment of B cells and further revealed the expansion of specific B cell subsets (Supplementary Figure 5A), as well as alterations in the myeloid compartment, notably an increase in macrophages with distinct M1- and M2-like signatures (Supplementary Figure 5B). In contrast, most other immune cell populations remained largely unchanged, including T lymphocytes, with $CD4^+$ and $CD8^+$ subsets showing no significant variation, except for regulatory T cells (Tregs), which were modestly enriched (Supplementary Figure 5C, 5D). Concomitantly, global immune and microenvironment scores were significantly increased (Supplementary Figure 5E). To validate this finding, we performed immunohistochemistry to quantify the expression of B lymphocyte and macrophage markers, B220 and CD68, respectively. Both markers were found to be significantly increased in the livers of old *Ptpn6*^{Ala457Thr} mice compared to old WT littermates but also as compared to young adult *Ptpn6*^{Ala457Thr} mice (Figure 6B, 6C). Experiments performed in 15–16-month-old female and male mice bearing a hepatocyte-specific invalidation of SHP-1 (*Ptpn6*$^{H\text{-}KO}$) and their littermates (*Ptpn6*$^{fl/fl}$) did not show a difference in B220 and CD68 expression (Supplementary Figure 6A–6F) suggesting that hepatocyte-specific deletion of SHP-1 alone is not sufficient to drive alterations in hepatic immune cell infiltration during aging.

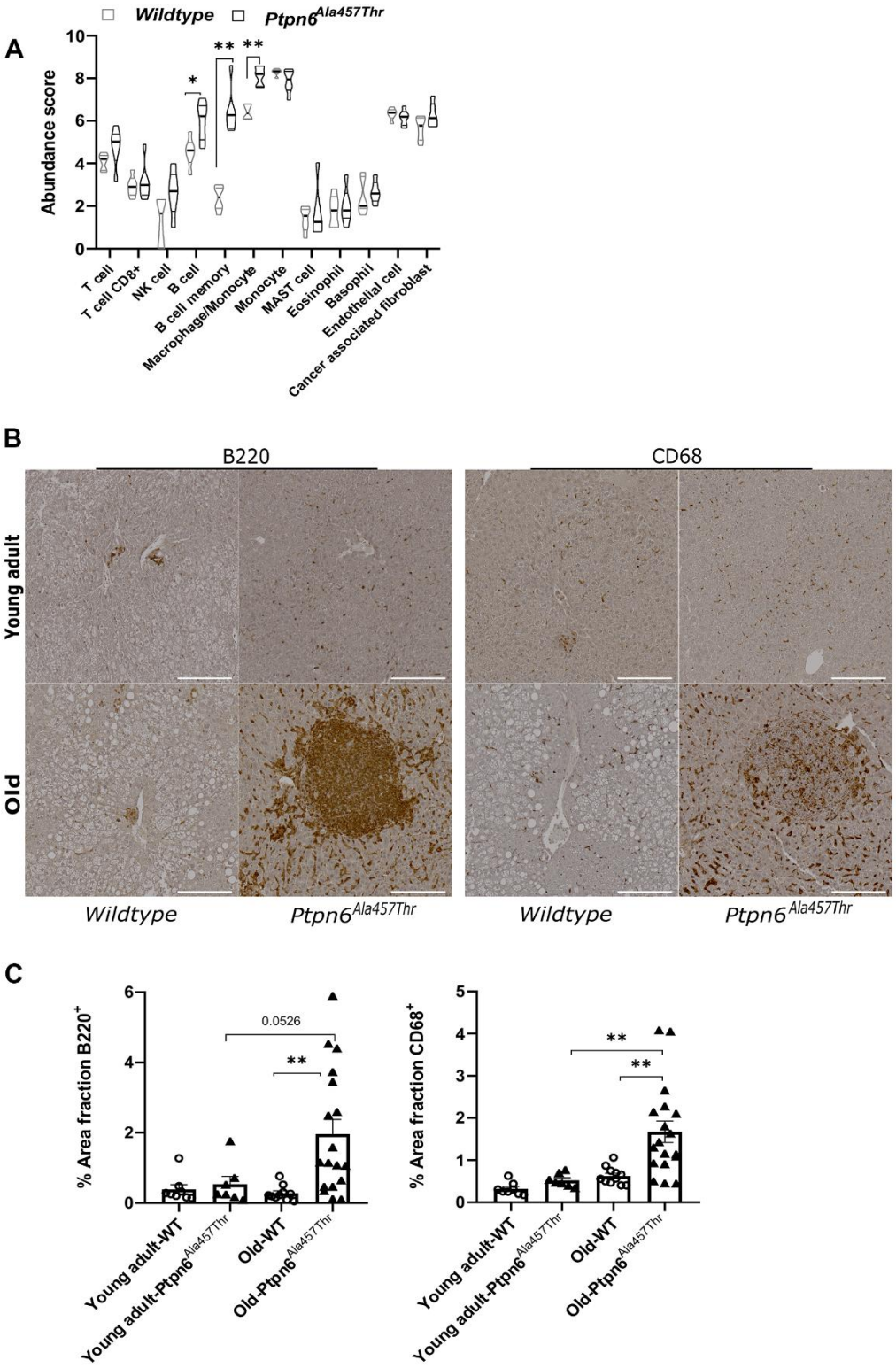

Figure 6. Age-related alterations in the presence of B cells and macrophages in livers of wildtype and *Ptpn6*^{Ala457Thr} mice. (**A**) Immune cell type deconvolution based on RNA-seq data estimating relative abundance of liver-resident and infiltrating immune cell populations (*n*=6 per group). (**B**) Representative immunohistochemistry images of liver sections stained for B220 (B cells) and CD68 (macrophages) in wildtype and *Ptpn6*^{Ala457Thr} young adult and old mice. Scale bar: 100 µm. (**C**) Quantification of B220^{+} and CD68^{+} area in liver sections from young adult and old wildtype and *Ptpn6*^{Ala457Thr} mice. Data are represented as mean ± SEM. Statistical significance was determined using unpaired two-tailed Student's t test and two-way ANOVA followed by Tukey's post hoc test, with **p* < 0.05, **p < 0.01, ****p* < 0.001. Sample sizes: young adult (YA) WT, n=8 and *Ptpn6*^{Ala457Thr}, n=7 Old WT, n=10-11 and *Ptpn6*^{Ala457Thr}, n=18.

Moreover, we measured the protein levels of the C-X-C motif chemokine ligand 13 (CXCL13), a known chemotactic factor involved in B cell migration [43]. Plasma CXCL13 levels were significantly elevated in old *Ptpn6*^{Ala457Thr} mice as compared to their WT counterparts (Figure 7A) supporting increased B cell chemotaxis. Hepatic CXCL13 levels also tended to be higher but this failed to reach statistical significance (Figure 7B). The anti-inflammatory cytokine interleukin 10 (IL-10) was also increased in the plasma of old *Ptpn6*^{Ala457Thr} mice (Figure 7C). IL-10 is known to be secreted by several immune cell types and increasing evidence highlights specific B lymphocyte subtypes as important IL-10 producers in various organs such as spleen and visceral adipose tissue [44, 45]. To determine the site of IL-10 production in old *Ptpn6*^{Ala457Thr} mice, we next measured the cytokine levels in the spleen and mesenteric white adipose tissue (mWAT). We found that IL-10 was significantly increased in both tissues in the old *Ptpn6*^{Ala457Thr} mice compared to their WT littermates (Figure 7D, 7E). In contrast, IL-10 levels were reduced in the liver of these mice as compared to their WT littermates (Figure 7F). Collectively, these findings suggest that the *Ptpn6*^{Ala457Thr} mutation is associated with a late-onset and progressive accumulation of intrahepatic B lymphocytes and macrophages, accompanied by changes in circulating and tissue levels of IL-10.

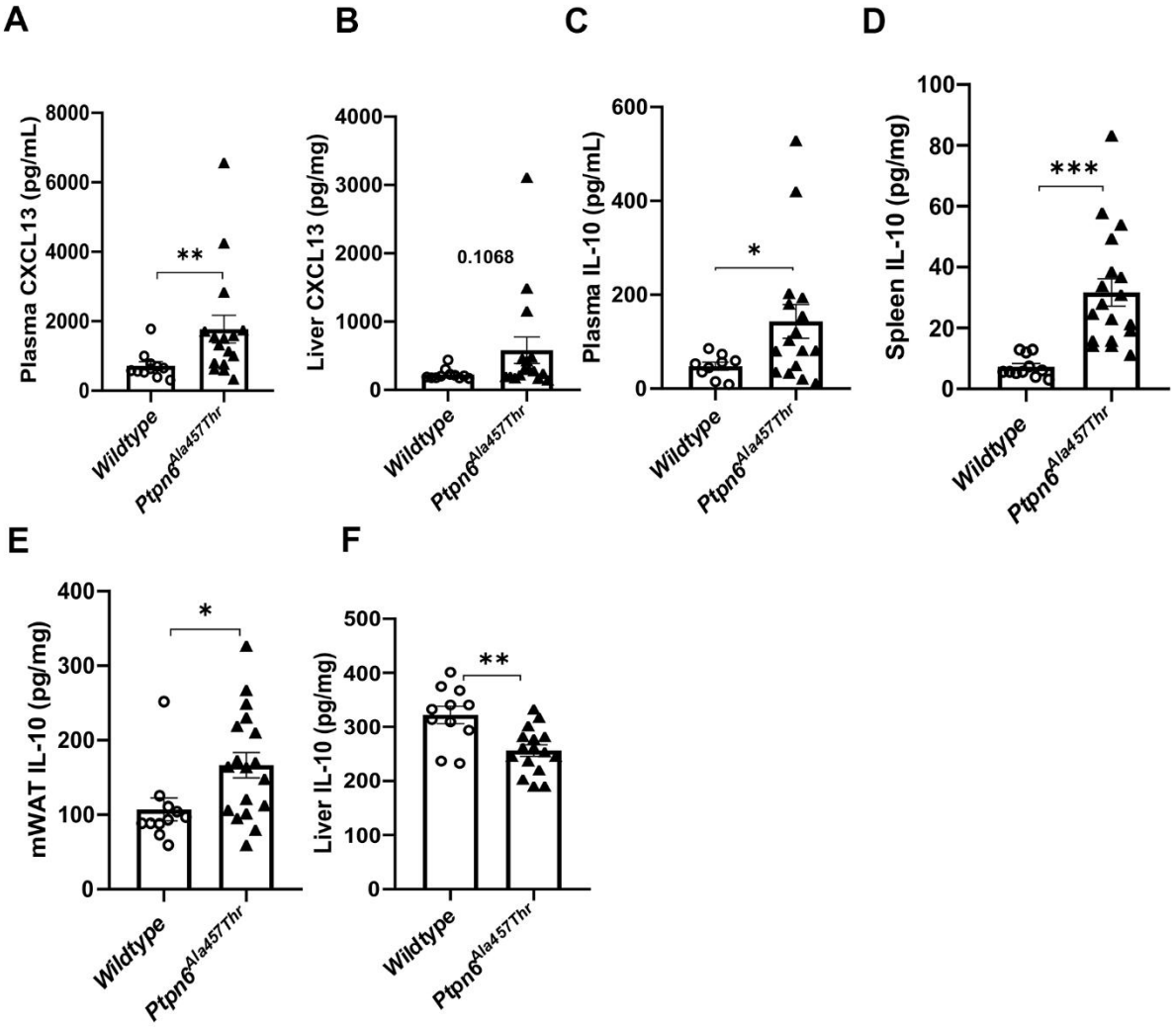

Figure 7. Changes in circulating and tissue levels of CXCL13 and IL-10 in wildtype and *Ptpn6*^{Ala457Thr} mice during aging. (**A**) Plasma and hepatic (**B**) CXCL13 levels measured using the Bio-Plex Pro Mouse Chemokine Assay Kit V. (**C**) Plasma IL-10 levels measured using the Bio-Plex Pro Mouse Chemokine Assay Kit V. (**D**) Splenic IL-10 levels measured using the DuoSet Mouse IL-10 Kit. (**E**) Mesenteric white adipose tissue IL-10 levels measured using the DuoSet Mouse IL-10 Kit. (**F**) Hepatic IL-10 levels measured using the Bio-Plex Pro Mouse Chemokine Assay Kit V. Data are represented as mean ± SEM. Statistical significance was determined using unpaired two-tailed Student's t test with *$p < 0.05$, **$p < 0.01$, ***$p < 0.001$. Sample sizes: Old WT, n=10-11 and *Ptpn6*^{Ala457Thr}, n=16-18.

DISCUSSION

In the present study, we characterized the immuno-metabolic effects of a recently reported human mutation (Ala455Thr, Ala457Thr in mice) in the *PTPN6* gene encoding SHP-1, which is associated with early-onset hereditary emphysema in patients [34]. Genetic introduction of this mutation in the mouse *Ptpn6* gene causes a modest but persistent reduction in tyrosine phosphatase activity, as determined by the increased phosphorylation of hepatic CEACAM1, which we have shown to be a canonical SHP-1 target [26]. Importantly, we show here that the *Ptpn6*^{Ala457Thr} mutation phenotypically manifests only in older mice (>16 months) and is associated with marked intrahepatic accumulation of immune cells and fibrosis, as revealed by substantial collagen deposition in the liver. Transcriptomic and immunohistochemical analyses further revealed that B cells and macrophages are the specific cell types that infiltrate the livers of aging *Ptpn6*^{Ala457Thr} mice. B220 staining showed the formation of tertiary lymphoid structures in the liver. These lymphoid aggregates form in non-hematopoietic organs, usually under pathological conditions such as cancer, autoimmune diseases, chronic inflammation, and aging [46].

Aging is associated with multi-layered alterations in liver biology that affect both parenchymal and non-parenchymal compartments, ultimately reshaping the hepatic microenvironment. Aging promotes hepatocyte senescence [47], mitochondrial dysfunction [48], impaired proteostasis [49], altered metabolic signaling and progressive extracellular matrix remodeling [50]. Importantly, aging also drives significant changes in the hepatic immune repertoire, including increased Kupffer cell activity [51], elevated IL-6 production [52], and chronic low-grade inflammation [53] (inflammaging), all of which contribute to a pro-inflammatory and pro-fibrogenic environment. In parallel, hepatic stellate cells in aged livers exhibit enhanced activation and increased expression of pro-fibrogenic mediators such as TGF-β, predisposing the liver to fibrosis [54]. In this context, the phenotype observed in aged *Ptpn6*^{Ala457Thr} mice is likely enabled by this preconditioned aging environment rather than solely driven by the mutation itself. Reduced SHP-1 activity may be adequately compensated in young mice but becomes insufficient in aged animals, where immune regulation is already compromised. Thus, aging may act as a permissive factor that unmasks the pathological consequences of partial SHP-1 dysfunction, facilitating the accumulation of B cells and macrophage subsets, as well as the progression towards fibrosis.

The aberrant intrahepatic B cell and macrophage infiltration and increased collagen deposition in the livers of old *Ptpn6*^{Ala457Thr} mice may be early signs of progressive liver dysfunction. Indeed, B cells have been shown to play key roles in the development of liver fibrosis. For example, B cell deficiency is protective in carbon tetrachloride (CCl4) induced liver damage, where histological analysis revealed markedly reduced collagen deposition in B cell-deficient mice [55]. In the absence of B cells, the ability of macrophages to clear damaged hepatocytes was enhanced, indicating that crosstalk between B cells and macrophages influence disease progression. Intestinal B cells have also been implicated in the development and progression of liver fibrosis by driving antigen-independent T-cell activation and IgA-FcR signaling [56]. B-cell activating factor (BAFF) deficient mice fed a high fat high cholesterol diet and treated with CCl4 showed reduced fibrosis progression compared to wildtype controls [57]. These mice also had fewer M1 proinflammatory macrophages in the liver, once again highlighting the role of B cells in fibrosis progression and their influence on macrophage polarization and activation.

We have identified increased STAT3 signaling as a potential mechanism underlying the aging-related liver fibrosis in *Ptpn6*^{Ala457Thr} mice. This is consistent with a previous report that the SHP-1 agonist SC-43 led to dephosphorylation and inhibition of STAT3 in hepatic stellate cells, inducing apoptosis and reducing fibrogenesis [58]. Another study demonstrated that SHP-1 negatively regulates epithelial-to-mesenchymal transition (EMT) in hepatocellular carcinoma by inactivating STAT3 signaling, particularly at the phosphorylated Tyr705 residue [39]. Interestingly, EMT is a process that involves the accumulation of extra-cellular matrix, contributing to fibrosis [59, 60]. Our transcriptomic analysis revealed that the IL-6-STAT3 pathway was activated in the liver of old mutant mice, and immunoblotting confirmed STAT3 activation as revealed by enhanced phosphorylation of STAT3 at Tyr705 and Ser727 in whole liver lysates of aged *Ptpn6*^{Ala457Thr} mice. Since STAT3 is broadly expressed in the liver and its expression levels and downstream effects vary depending on the cell type [61], it is important to determine the cellular origin of STAT3 activation. Given that phosphorylation of STAT3 is not different between primary hepatocytes isolated from aged *Ptpn6*^{Ala457Thr} and WT mice, this suggests that increased STAT3 phosphorylation mostly reflects activation in the infiltrated immune cells of these mice. More studies will be needed to determine more precisely the contribution of intrahepatic B cells and/or macrophages to STAT3 activation and thus to liver fibrogenesis in aged *Ptpn6*^{Ala457Thr} mice.

It has been reported that *Ptpn6*$^{Spin/Spin}$ mice carrying a recessive *Ptpn6* mutation induced by N-ethyl-N-

nitrosourea (ENU) mutagenesis also develop an autoimmune and inflammatory phenotype when reaching 6 weeks of age and that this mutation is associated with splenomegaly [36]. Consistent with the *Ptpn6*$^{Spin/Spin}$ phenotype, *Ptpn6*^{Ala457Thr} mice had an enlarged spleen. However, the phenotypic impact of the *Ptpn6*^{Ala457Thr} mutation only manifested during aging. Accordingly, we also observed aberrant hepatic immune cell infiltration in old but not in young adult *Ptpn6*^{Ala457Thr} mice. We believe that these liver perturbations are more likely associated with reduced SHP-1 function in immune cells than in hepatocytes, as comparable immune changes were not detected in hepatocyte-specific SHP-1 knockout mice [27]. Nonetheless, the contribution of hepatocyte-intrinsic mechanisms cannot be excluded, and the phenotype may also reflect crosstalk between infiltrating immune cells and hepatocytes or other parenchymal cells.

Our findings support a model of liver injury that occurs independently of obesity, steatosis, or insulin resistance. In aged mice, reduced SHP-1 function in *Ptpn6*^{Ala457Thr} mutant mice was actually associated with lower adiposity, improved glucose metabolism and liver insulin action despite increased hepatic B cell and macrophage infiltration. The beneficial metabolic phenotype of these mice was somewhat surprising given that previous studies have implicated a role of B cells as immune mediators of insulin resistance and altered glucose metabolism, especially in the context of obesity. Indeed, B cells have been shown to accumulate and promote insulin resistance through the activation of proinflammatory macrophages in visceral adipose tissue in a mouse model of obesity [62]. Furthermore, aging-associated changes in B2 cell adaptive immunity, driven by increased B-cell-specific transcriptional coactivator OcaB expression and IgG production, promote glucose intolerance and fat accumulation [63]. On the other hand, B-1a cells, which produce IL-10 in adipose tissue, protect against obesity-induced insulin resistance, and their loss promotes metabolic dysfunction [64]. Moreover, natural antibodies-producing B-1b cells reduce adipose tissue inflammation and improve glucose metabolism in obesity, highlighting their protective role in both mice and humans [65]. Similarly, adipose-resident regulatory B cells producing IL-10 help maintain metabolic homeostasis, and their dysfunction promotes inflammation and insulin resistance in obesity [66]. Interestingly, we have observed enhanced IL-10 production in visceral adipose tissue (mWAT) and spleen of aged *Ptpn6*^{Ala457Thr} mice, which may contribute to the preserved metabolic homeostasis of mutant mice during aging. Indeed, not only adipose tissue resident B-1 cells but also innate-like spleen-supplied B cells have been shown to promote metabolic benefits in diet-induced obesity through releasing IL-10 [44, 45]. This enhanced IL-10 production in peripheral tissues may contribute to the paradoxical finding of improved liver insulin action and systemic glucose metabolism despite the development of liver fibrosis in aged *Ptpn6*^{Ala457Thr} mice. The overall immunometabolic phenotyping of *Ptpn6*^{Ala457Thr} mutation thus demonstrates that we can disentangle the infiltration of B cells and macrophages, and the resulting inflammation and fibrosis, to the development of hepatic insulin resistance and whole-body glucose control during aging in mice. Further studies are needed to clarify the specific roles of infiltrating B cell subtypes and macrophages in driving the immunometabolic phenotypes of aged *Ptpn6*^{Ala457Thr} mice. Depleting B cells using a murine anti-CD20 antibody [56] or macrophages using clodronate liposomes [67] in old *Ptpn6*^{Ala457Thr} mice will provide additional insights on how these immune populations contribute to their unique phenotypes.

Immune dysfunction and insulin resistance are widely recognized hallmarks of aging, where chronic low-grade inflammation and age-associated declines in immune homeostasis contribute to metabolic dys-regulation and impaired insulin action in older organisms [53, 68]. The partial loss of SHP-1 function in both immune and metabolic cells in *Ptpn6*^{Ala457Thr} mice was found to be associated with a complex liver phenotype, with both enhanced hepatic inflammation and fibrosis concomitantly observed with augmented insulin signaling, which might appear contradictory. However, SHP-1 loss differently affects immune cells: deletion in B cells perturbs B cell development and promotes autoimmunity [69], macrophage-specific SHP-1 deficiency enhances pro-inflammatory cytokine production and effector function [70], neutrophilspecific SHP-1 loss leads to hyperinflammatory responses [71] and SHP-1 deficiency in T cells alters activation and survival phenotypes [72]. In hepatocytes and other insulin-responsive tissues, SHP-1 deficiency relieves inhibitory control of insulin receptor pathways. Indeed, we have shown that SHP-1 is a major negative regulator of insulin signaling in liver [26]. We reported that viable motheaten *Ptpn6*$^{me\text{-}v/me\text{-}v}$ mice, which carry a whole-body dysfunctional SHP-1 protein that retains about 20% of wildtype activity [73], have enhanced hepatic and muscle insulin receptor signaling to the IRS1-PI3K-Akt pathway. These beneficial hepatic phenotypes were reproduced after downregulation of SHP-1 activity in liver of normal mice by adenoviral expression of a catalytically inert mutant of SHP-1, or after small hairpin RNA-mediated SHP-1 silencing [26]. Concomitantly, obese mice bearing hepatocyte-specific *Ptpn6* deletion showed improved hepatic insulin sensitivity and were protected from inflam-mation and hepatocellular damage [27] Together, these

studies indicate that enhanced insulin signaling in aged *Ptpn6*^{Ala457Thr} mice reflects tissue-specific relief of SHP-1-mediated inhibition rather than a global anti-aging effect, demonstrating that inflammation and improved insulin signaling can coexist as distinct, tissue-specific consequences of partial SHP-1 dysfunction in the aging environment.

It is important to note that the present study was performed only in male *Ptpn6*^{Ala457Thr} mice, and potential sex-specific differences in immunometabolic and fibrotic phenotypes cannot be excluded. Future studies including female mice will be essential to determine whether the observed effects of the *Ptpn6*^{Ala457Thr} mutation are generalizable across sexes.

Collectively, the present findings support a model in which systemic, mild SHP-1 dysfunction is associated with a late-onset phenotype characterized by the accumulation of B cells and macrophages in the liver, leading to increased collagen deposition and fibrosis, but without exacerbating systemic glucose homeostasis or liver steatosis. Both immune cells and insulin-responsive tissues rely on tightly regulated signaling cascades to maintain homeostasis, and dysregulation of SHP-1 activity may disrupt immunometabolic balance. Our data offer human-relevant insights, as the *Ptpn6*^{Ala457Thr} mutation was originally identified in a French-Canadian family. Elucidating the mechanisms by which SHP-1 modulates immunometabolic pathways may reveal novel therapeutic strategies to mitigate age-associated inflammation and insulin resistance as well as hepatic diseases. Our findings further provide new insight into how mild, chronic immune dysregulation can contribute to liver fibrosis independently of traditional metabolic risk factors.

MATERIALS AND METHODS

Animals

C57Bl/6N male *Wildtype* and mutants *Ptpn6*^{Ala457Thr} mice were kindly provided by Dr. Mathieu Morissette (Institut Universitaire de Cardiologie et de Pneumologie de Québec, Canada). Briefly, Male and female mice of C57BL/6N background carrying the specific mutation in the *Ptpn6* gene were generated using CRISPR/Cas 9 technology, where guanine was replaced by an adenine at position 1363 (McGill Integrated Core for Animal Modeling) as previously described [74]. This change caused an alanine to threonine switch at position 457 in the amino acidic sequence of SHP-1 protein, corresponding to the amino acid at position 455 in humans. Heterozygote male founders were crossed with wildtype C57BL/6N females and F1 heterozygote males with wildtype C57BL/6N females up to F6 to generate *Ptpn6*^{Ala457Thr} heterozygote pups for experimentations. The mouse colony is maintained by crossing *Ptpn6*^{Ala457Thr} heterozygote males with wildtype females. Male heterozygote and wildtype littermates were used for experimentation. Animals were single-housed in ventilated cages at a humidity of 40-50% and a temperature of 22°C on a 12h dark-light cycle with ad libitum standard CHOW diet. Food intake was measured once per week over a 1-month period. Young adult Janus (5.6 months old) and old (16-19 months old) mice were fasted for 6h, followed by an oral glucose tolerance test (OGTT) with a dose of 1 mg of glucose per gram of body weight. Euthanasia was performed one week after the OGTT. Mice were fasted 6h and injected intravenously with saline or 3.8 U/Kg insulin (HI0213, Lilly) 5 min prior sacrifice. Hepatocyte-specific SHP-1 knockout mice (*Ptpn6*$^{H\text{-}KO}$) and control floxed SHP-1 mice (*Ptpn6*$^{fl/fl}$), as previously described [24], were used at 15-16 months of age. All animals were euthanatized by cardiac puncture under isoflurane anesthesia and cervical dislocation before tissue collection. All manipulations were approved by the Animal Ethics Committee of Université Laval (CPAUL 2019-26, 2022-1086 and 2022-1079) and complied with the Canadian Council on Animal Care guidelines (CCAC).

Biochemical analyses

ELISA assays were used to measure insulin (Alpco Mouse Ultrasensitive Insulin kit Cat# 80-INSMSU-E01) according to the manufacturer's instructions. Plasma and liver triglycerides were measured using the Infinity Triglycerides Thermo Scientific kit according to the manufacturer's instructions. Briefly, liver lipids were extracted using a modified Folch method [75]. In summary, 45-55 mg of frozen liver tissue was homogenized in chloroform:methanol (2:1), followed by the addition of 0.73% NaCl to induce phase separation. After centrifugation, the lower organic phase containing lipids was collected, dried under nitrogen, and stored at -20°C or resuspended in appropriate solvents for further analysis. Bio-Plex Pro Mouse Chemokine Assay Kit V (Cat# 12002798, Bio-Rad) was used to measure plasma and liver IL-10 and CXCL13 levels according to the manufacturer's instructions. Splenic and mesenteric white adipose tissue IL-10 levels were determined using the DuoSet Mouse IL-10 Kit (Cat# DY417-05, R&D Systems) following the manufacturer's instructions.

Immunoblotting

20-40 mg of liver, gastrocnemius muscle and mesenteric white adipose tissue were powdered with liquid nitrogen and then homogenized 10 sec using a bead mill homogenizer (VWR, USA) in 500 µL of ice-

cold lysis buffer [150 mM NaCl (BP358-212; Fisher BioReagents), 20 mM Tris-HCL pH 7.5 (T5941; Sigma-Aldrich), 10% Glycerol (G5516; Sigma-Aldrich), 5 mM EGTA (E4378, Sigma-Aldrich), 0.5 mM EDTA (BP120-500; Fisher BioReagents), 2 mM Na_3VO_4 (S6508-50G; Sigma-Aldrich), 10 mM NaF (S6776-100G; Sigma-Aldrich), 1% Triton (9036-19-5, Sigma-Aldrich), 0.1% SDS (L3771; Sigma-Aldrich), 80 mM β-glycerophosphate (G5422, Sigma-Aldrich), 0.1 mM $Na_4P_2O_7$ (221368-100G; Sigma-Aldrich), 0.1 mM PMSF (P7626-5G; Sigma-Aldrich) and 1X protease inhibitors cocktail (P8340, Sigma-Aldrich)]. Similarly, primary hepatocytes were washed with PBS and lysed in ice-cold lysis buffer. Lysates were clarified by centrifugation at 16,000 × *g* for 10 min at 4°C and the protein concentrations were measured with a BCA assay (Thermo Fisher Scientific, Burlington, Canada). Tissue and cell lysates were denatured in SDS sample buffer and submitted to SDS-PAGE followed by transfer on nitrocellulose membranes (Amersham Protran, Germany). Membranes were blocked for 1 hour at room temperature in 5% milk in TBST [20 mM Tris-HCl pH 7.5, 0.15 mM NaCl, and 0.1% Tween-20 (BP337; Fisher BioReagents)] or, for phosphorylated proteins, in 5% bovine serum albumin (A9647-100G; Sigma-Aldrich) in TBST, and then incubated with the primary antibody overnight at 4°C. After washing in TBST, the membranes were incubated with HRP-conjugated secondary antibodies for 1 h at room temperature. The detection was performed with an ECL reagent (Millipore, Etobicoke, Canada). ChemiDoc MP Imager and Image Lab software (version 6.1) were used to acquire and analyze images. The following antibodies were used: AKT (dilution, 1:2000; Cell Signaling Technology, 9272), pAKT (Thr308) (dilution, 1:800; Cell Signaling Technology, 9275S), pAKT (Ser473) (dilution, 1:1000; Cell Signaling Technology, 9271), Actin (dilution, 1:3000; Millipore, MAB1501), eEF2 (dilution, 1:2000; Cell Signaling Technology, 2332), STAT3 (dilution, 1:1000; Cell Signaling Technology, 9132), pSTAT3 (Tyr705) (dilution, 1:1000; Cell Signaling Technology, 9131), pSTAT3 (Ser727) (dilution, 1:1000; Cell Signaling Technology, 9134), OXPHOS (dilution, 1:1000; Abcam, MS 604-300), CEACAM1 (dilution 1:1000; previously described [76]), PY20 (dilution, 1:1000; Abcam ab1021), 4G10 (dilution, 1:1000; Millipore 05-321) and SHP-1 (dilution, 1:1000; R&D Systems, AF1878). Secondary antibodies were purchased from Jackson Immuno-research Laboratory (Cat#705-035-147, Cat #111-035-144 and Cat#115-035-546).

Immunoprecipitation

For immunoprecipitation, 1 mg of total protein extracted from livers using lysis buffer containing 20 mM Tris-HCl pH 7.5, 140 mM NaCl, 1 mM $CaCl_2$ (C3881, Sigma-Aldrich), 1 mM $MgCl_2$ (7791-18-6, Sigma-Aldrich), 10 mM NaF, 1% NP-40 (I3021, Sigma-Aldrich), 10% glycerol, 2 mM Na_3VO_4, 1 mM PMSF, and 1X protease inhibitor cocktail was incubated overnight at 4°C with an anti-CEACAM1 antibody. The next day, the samples containing lysate and antibody were incubated for 2 hours with protein A sepharose beads (17-0469-01.GE Healthcare Bio-Sciences), followed by five washes with PBS containing 1% NP-40, 2 mM Na_3VO_4, and protease inhibitors. Beads were boiled in 1× Laemmli sample buffer, and immunoblot analysis was performed.

Hepatocyte isolation and culture

Primary hepatocytes were isolated from 15- to 21-month-old *wildtype* and *Ptpn6*^{Ala457Thr} female and male mice. Animals were handled in accordance with the guidelines of the Canadian Council on Animal Care, and protocols were approved by the Animal Ethics Committee of Université Laval (CPAUL). The hepatocytes were isolated using the two-step collagenase perfusion method [77]. Briefly, the liver was infused with 50 ml of perfusion buffer (0.51 mM CaCl2, 137 mM NaCl, 7 mM KCl (P9541, Sigma-Aldrich), 0.7 mM Na_2HPO_4 (71643, Sigma-Aldrich), and 10 mM Hepes (H3375, Sigma-Aldrich) via the vena cava inferior followed by 50 ml of perfusion buffer containing 20 mg collagenase type I from Clostridium histolyticum (C0130, Sigma-Aldrich). After the perfusion, the liver was excised and disintegrated in cell attachment medium [M199 medium supplemented with 10% FBS, 1% penicillin/streptomycin (P0781, Sigma-Aldrich), 500 nM dexamethasone (D1756, Millipore), 10 nM insulin, 200 nM thyroid hormone (T2877, Sigma-Aldrich), 0.1% bovine serum albumin (A9647, Sigma-Aldrich) and 1× Glutamax (35050, Gibco)]. The cellular suspension was centrifuged at 400 rpm for 2 min. The cell viability was measured by trypan blue exclusion method. The cells were resuspended in cell attachment media and seeded on the cell culture plates. Serum-free culture medium (M199 supplemented with 1× Glutamax, 1% penicillin/streptomycin and 100 nM dexamethasone) was added 2h after plating to remove unattached cells. The next day the hepatocytes were used for experiments.

Oxygen consumption

Primary mouse hepatocytes were seeded in a collagen type I coated Seahorse 24-well plate at a density of 20,000 cells per well. Twenty-four hours later, cells were washed three times with Seahorse XF medium [DMEM without phenol red supplemented with 2mM pyruvate (S8636, Sigma-Aldrich), 4 mM L-glutamine

(25030-081, Gibco), 5.5 mM glucose (G8270, Sigma-Aldrich)], and the Seahorse Mito Stress protocol was run according to the manufacturer's instructions. Oxygen consumption was assessed by the sequential addition of oligomycin (2 μM), carbonyl cyanide *p*-trifluoromethoxyphenylhydrazone (FCCP; 2 μM), and a mix of rotenone (1 μM) and antimycin A (1 μM). The oxygen consumption rate (OCR) measurements were normalized to total DNA content, and parameters were calculated using the Seahorse Wave Desktop software from Agilent.

RNA isolation and sequencing

Total RNA was isolated from liver tissue of six wildtype and six *Ptpn6*^{Ala457Thr} mice (16-19 months old), randomly selected, using the Zymo Research kit according to the manufacturer's instructions. The purity and quantity of RNA were assessed using BioDrop spectrophotometer. Samples with RNA integrity number (RIN) > 6.5 were submitted to the Génome Québec Innovation Centre (Montreal, QC, Canada) for library preparation and sequencing. The samples were sequenced on an Illumina NovaSeq PE100 mRNA Library Prep Kit platform yielding an average of 25 million reads per sample. Raw sequencing data were quality-checked using FastQC (v0.12.0) [78], and Trim Galore (v0.6.10) [79] was used to remove adapter sequences and low-quality bases. Processed reads were aligned to the GRCm39 mouse reference genome using Kallisto (v0.46.1) [80]. Gene-level counts were obtained via the tximport package (v1.34.0) [81], and differential expression analysis was conducted using DESeq2 (v1.46.0) [82]. Genes with adjusted p-values < 0,05 were considered significantly differentially expressed. Pathway enrichment analysis was performed for HALLMARK pathways using the GSVA R package (v2.0.5) [83–85]. Immune cells were quantified using mMCPCounter and xCell [42] methods from the immunedecov R package (v2.1.0) [41, 86]. For the xCell algorithm mouse genes were mapped to mouse orthologs using biomaRt R package (v2.68.0) [87, 88], retaining one-to-one orthologs where possible. Human common aging and inflammaging gene sets were derived from a genome-wide CRISPRi screen [37] defined based on heritability enrichment from association studies. Human genes were mapped to mouse orthologs as described above and the resulting mouse gene sets were used for downstream transcriptomic analyses.

RT-qPCR

Total RNA was isolated as described above. Two micrograms of total RNA were reverse-transcribed using the High-capacity cDNA reverse transcription kit (Applied Biosystems) with random primers. The resulting cDNA was diluted, and the expression of the transcripts was quantified using the Advanced qPCR master mix (Wisent). Gene expression was normalized to the reference gene *B2m*. The sequences of the primers used were as follows: *Ptpn6a* (forward: 5'- AGACAAAC TGTTCCCTCCAC-3', reverse: 5'-CAGGGTCTCTGC ATCAGG-3'), *Ptpn6b* (forward: 5'-TGAAGGTCTGGA TCCCTGAA-3', reverse: 5'-CTGAGGTCCCGGTG AAAC-3'), *B2m* (forward: 5'-GGGTGGAACTGTGTT ACGTAG-3', reverse: 5'-TGGTCTTTCTGGTGCTTG TC-3'), *Cdkn1a* (forward: 5'-GACAAGAGGCCCAGT ACTTCC-3', reverse: 5'-CTTGCAGAAGACCAATC TGCG-3').

Liver histology and immunohistochemistry

Liver tissue samples were fixed for 48 hours in 10% formalin at 4°C. Tissues were next dehydrated, embedded in paraffin, and cut into 10-μm-thick sections. Sections were stained with hematoxylin and eosin (H&E) as well as with Picrosirius red. All pictures were acquired with the Axio Observer.Z1 using a Plan Apochromat 20x/0.8 M27 objective (Zeiss, Germany) and were reviewed and scored by a pathologist. Steatosis and inflammation were assessed on H&E-stained slides. The total amount of steatosis was measured as the percentage of hepatocytes containing lipid droplets. The inflammation score was determined by counting the number of inflammatory foci containing more than 5 immune cells per high-power field. Fibrosis stage was scored on Picrosirius red-stained sections using a five-point scale: 0 (none), 1A (Zone 3, slight perisinusoidal fibrosis), 1B (Zone 3, moderate perisinusoidal fibrosis), 1C (portal/periportal fibrosis), 2 (perisinusoidal and periportal fibrosis), 3 (bridging fibrosis), and 4 (cirrhosis) [89]. Immunohistochemistry (IHC) was performed on paraffin-embedded tissue sections (10 μm). Sections were deparaffinized in toluene, rehydrated through graded ethanol, and subjected to antigen retrieval by heating in 10 mM citrate (C8532-100G; Sigma-Aldrich) buffer (pH 6.0) for 10 minutes, followed by cooling at room temperature for 30 minutes. Endogenous peroxidase activity was quenched using 3% hydrogen peroxide (H1009; Sigma-Aldrich) in distilled water for 10 minutes. Tissue sections were then blocked using TBST and 5% goat serum for 1 hour at room temperature. Primary antibodies against B220, (dilution 1:200, Cell Signaling Technology 70257S) and CD68 (dilution 1:600, Cell Signaling Technology 97778T) were applied and incubated overnight at 4°C in a humidified chamber. Negative control using IgG Isotype control antibody was included (Invitrogen, 02-6102). Following primary antibody incubation, sections were washed and incubated with HRP-

conjugated secondary antibodies (SignalStain® Boost IHC Detection Reagent, CST 8114S) for 30 minutes at room temperature. Immunoreactivity was visualized using 3,3′-diaminobenzidine (DAB) substrate, and sections were counterstained with hematoxylin, dehydrated, and mounted. Image analysis was carried out using ImageJ software v1.53 (NIH, Bethesda, MD, USA).

Quantification and statistical analysis

All data are reported as mean ± SEM. Statistical analysis was performed using the GraphPad Prism 8 software (https://graphpad.com). We used a two-tailed Student's *t*-test, a Two-way ANOVA, a Three-way ANOVA or a mixed model for repeated measures, followed by a Tukey post-hoc test. The number of biological repeats included in the experiments is mentioned in the figure legends.

Materials availability

Further information and requests for resources and reagents should be directed to and will be fulfilled by the corresponding author, André Marette (andre.marette@criucpq.ulaval.ca).

Data availability statement

The RNA-seq data discussed in Figure 5 of this manuscript have been deposited in NCBI's Gene Expression Omnibus [90] and are accessible through GEO Series accession number GSE310012 https://www.ncbi.nlm.nih.gov/geo/query/acc.cgi?acc=GSE310012.

Abbreviations

SHP-1: Src homology region 2-containing phosphatase 1; PTPN6: Protein tyrosine phosphatase non-receptor type 6; STAT3: Signal transducer and activator of transcription 3; ITIM: immunoreceptor tyrosine-based inhibition motif; PIR-B: paired immunoglobulin-like receptor B; SIRPα: signal regulatory protein alpha; ITAM: immunoreceptor tyrosine-based activation motif; FcRs: immunoglobulin Fc receptors; JAKs: Janus kinases; STAT: Signal transducer and activator of transcription; CSF1R: colony-stimulating factor 1; TCR: T cell receptor; Lck: lymphocyte specific protein tyrosine kinase; ZAP-70: zeta-chain of T cell receptor associated protein kinase 70; LAT: linker for activation of T cells; SLP-76: SH2-domain-containing leukocyte protein of 76 kDa; BCR: B cell receptor; CD22: cluster of differentiation 22; CD72: cluster of differentiation 72; FcγRIIB: Fc gamma receptor IIB; CEACAM1: carcinoembryonic antigen-related cell adhesion molecule-1; HFD: high-fat diet; IL-3: interleukin-3; IL-6: interleukin-6; RANTES: regulated upon activation, normal T cell expressed, and secreted; TNFα: tumor necrosis factor; MASLD: metabolic dysfunction-associated steatotic liver disease; WT: wildtype; OGTT: oral glucose tolerance test; CPAUL: Animal Ethics Committee of Université Laval; CCAC: Canadian Council on Animal Care guidelines; OCR: oxygen consumption rate; CXCL13: C-X-C motif chemokine ligand 13; IL-10: interleukin 10; mWAT: mesenteric white adipose tissue; iWAT: inguinal adipose tissue; BAT: brown adipose tissue; Gastroc: gastrocnemius; CCl4: carbon tetrachloride; EMT: epithelial-to-mesenchymal transition; ENU: N-ethyl-N-nitrosourea; H&E: hematoxylin and eosin; Akt: protein kinase B; OXPHOS: oxidative phosphorylation; GSEA: gene set enrichment analysis; MCP-counter: microenvironment cell populations-counter; Tregs: regulatory T cells; CRISPRi: CRISPR interference; RT-qPCR: reverse transcription quantitative polymerase chain reaction; cDNA: complementary DNA; RIN: RNA integrity number; GSVA: gene set variation analysis; DESeq2: differential expression sequencing 2; IHC: immuno-histochemistry; DAB: 3,3′-diaminobenzidine; HRP: horseradish peroxidase; ECL: enhanced chemi-luminescence; BCA: bicinchoninic acid assay; PBS: phosphate-buffered saline; SDS: sodium dodecyl sulfate; SDS-PAGE: sodium dodecyl sulfate–polyacrylamide gel electrophoresis; TBST: Tris-buffered saline with Tween-20; EGTA: ethylene glycol-bis(β-aminoethyl ether)-N,N,N′,N′-tetraacetic acid; EDTA: ethylenediaminetetraacetic acid; PMSF: phenylmethylsulfonyl fluoride; eEF2: eukaryotic elongation factor 2; FBS: fetal bovine serum; DMEM: Dulbecco's Modified Eagle Medium; FCCP: carbonyl cyanide p-trifluoromethoxyphenylhydrazone; IRS1: insulin receptor substrate 1; PI3K: phosphoinositide 3-kinase; IgA: immunoglobulin A; IgG: immunoglobulin G; TGF-β: transforming growth factor beta; NIH: National Institutes of Health.

ACKNOWLEDGMENTS

We would like to thank Christine Dallaire, Joanie Morissette, Jacinthe Julien, and Geneviève Guèvremont for their valuable assistance with animal handling and care.

AUTHOR CONTRIBUTIONS

BLL, AK, MS, KB, ML, MM and AM conception of the study. BLL, MS, KB performed the experiments. BLL, MS, KB, AK, AG, MP data analysis. BLL, MS, KB and AM wrote the manuscript. All authors revised the manuscript and approved the final version.

CONFLICTS OF INTEREST

The authors declare that they have no conflicts of interest.

ETHICAL STATEMENT

The study protocol was reviewed and approved by the Institutional Animal Care and Use Committee of the Laval University (CPAUL 2019-26, 2022-1086 and 2022-1079). All experiments were performed in accordance with the institutional guidelines on animal experimentation.

FUNDING

This work was supported by a Canadian Institutes of Health Research (CIHR) Foundation grant (FDN-143247) to A.M. A.M. holds a Pfizer research fund in the pathogenesis of insulin resistance and cardio-vascular diseases.

REFERENCES

1. Nesterovitch AB, Gyorfy Z, Hoffman MD, Moore EC, Elbuluk N, Tryniszewska B, Rauch TA, Simon M, Kang S, Fisher GJ, Mikecz K, Tharp MD, Glant TT. Alteration in the gene encoding protein tyrosine phosphatase nonreceptor type 6 (PTPN6/SHP1) may contribute to neutrophilic dermatoses. Am J Pathol. 2011; 178:1434–41. https://doi.org/10.1016/j.ajpath.2010.12.035 PMID:21406173

2. Wu C, Sun M, Liu L, Zhou GW. The function of the protein tyrosine phosphatase SHP-1 in cancer. Gene. 2003; 306:1–12. https://doi.org/10.1016/s0378-1119(03)00400-1 PMID:12657462

3. Stone RL, Dixon JE. Protein-tyrosine phosphatases. J Biol Chem. 1994; 269:31323–6. https://doi.org/10.1016/S0021-9258(18)31694-6 PMID:7989293

4. Plutzky J, Neel BG, Rosenberg RD, Eddy RL, Byers MG, Jani-Sait S, Shows TB. Chromosomal localization of an SH2-containing tyrosine phosphatase (PTPN6). Genomics. 1992; 13:869–72. https://doi.org/10.1016/0888-7543(92)90172-o PMID:1639416

5. Abram CL, Lowell CA. Shp1 function in myeloid cells. J Leukoc Biol. 2017; 102:657–75. https://doi.org/10.1189/jlb.2MR0317-105R PMID:28606940

6. Lorenz U. SHP-1 and SHP-2 in T cells: two phosphatases functioning at many levels. Immunol Rev. 2009; 228:342–59. https://doi.org/10.1111/j.1600-065X.2008.00760.x PMID:19290938

7. Maeda A, Kurosaki M, Ono M, Takai T, Kurosaki T. Requirement of SH2-containing protein tyrosine phosphatases SHP-1 and SHP-2 for paired immunoglobulin-like receptor B (PIR-B)-mediated inhibitory signal. J Exp Med. 1998; 187:1355–60. https://doi.org/10.1084/jem.187.8.1355 PMID:9547347

8. Timms JF, Carlberg K, Gu H, Chen H, Kamatkar S, Nadler MJ, Rohrschneider LR, Neel BG. Identification of major binding proteins and substrates for the SH2-containing protein tyrosine phosphatase SHP-1 in macrophages. Mol Cell Biol. 1998; 18:3838–50. https://doi.org/10.1128/MCB.18.7.3838 PMID:9632768

9. Roach TI, Slater SE, White LS, Zhang X, Majerus PW, Brown EJ, Thomas ML. The protein tyrosine phosphatase SHP-1 regulates integrin-mediated adhesion of macrophages. Curr Biol. 1998; 8:1035–8. https://doi.org/10.1016/s0960-9822(07)00426-5 PMID:9740804

10. Ben Mkaddem S, Hayem G, Jönsson F, Rossato E, Boedec E, Boussetta T, El Benna J, Launay P, Goujon JM, Benhamou M, Bruhns P, Monteiro RC. Shifting FcγRIIA-ITAM from activation to inhibitory configuration ameliorates arthritis. J Clin Invest. 2014; 124:3945–59. https://doi.org/10.1172/JCI74572 PMID:25061875

11. David M, Chen HE, Goelz S, Larner AC, Neel BG. Differential regulation of the alpha/beta interferon-stimulated Jak/Stat pathway by the SH2 domain-containing tyrosine phosphatase SHPTP1. Mol Cell Biol. 1995; 15:7050–8. https://doi.org/10.1128/MCB.15.12.7050 PMID:8524272

12. Klingmüller U, Lorenz U, Cantley LC, Neel BG, Lodish HF. Specific recruitment of SH-PTP1 to the erythropoietin receptor causes inactivation of JAK2 and termination of proliferative signals. Cell. 1995; 80:729–38. https://doi.org/10.1016/0092-8674(95)90351-8 PMID:7889566

13. Kozlowski M, Larose L, Lee F, Le DM, Rottapel R, Siminovitch KA. SHP-1 binds and negatively modulates the c-Kit receptor by interaction with tyrosine 569 in the c-Kit juxtamembrane domain. Mol Cell Biol. 1998; 18:2089–99. https://doi.org/10.1128/MCB.18.4.2089 PMID:9528781

14. Yi T, Ihle JN. Association of hematopoietic cell

phosphatase with c-Kit after stimulation with c-Kit ligand. Mol Cell Biol. 1993; 13:3350–8. https://doi.org/10.1128/mcb.13.6.3350-3358.1993 PMID:7684496

15. Chen HE, Chang S, Trub T, Neel BG. Regulation of colony-stimulating factor 1 receptor signaling by the SH2 domain-containing tyrosine phosphatase SHPTP1. Mol Cell Biol. 1996; 16:3685–97. https://doi.org/10.1128/MCB.16.7.3685 PMID:8668185

16. Chiang GG, Sefton BM. Specific dephosphorylation of the Lck tyrosine protein kinase at Tyr-394 by the SHP-1 protein-tyrosine phosphatase. J Biol Chem. 2001; 276:23173–8. https://doi.org/10.1074/jbc.M101219200 PMID:11294838

17. Plas DR, Johnson R, Pingel JT, Matthews RJ, Dalton M, Roy G, Chan AC, Thomas ML. Direct regulation of ZAP-70 by SHP-1 in T cell antigen receptor signaling. Science. 1996; 272:1173–6. https://doi.org/10.1126/science.272.5265.1173 PMID:8638162

18. Brockdorff J, Williams S, Couture C, Mustelin T. Dephosphorylation of ZAP-70 and inhibition of T cell activation by activated SHP1. Eur J Immunol. 1999; 29:2539–50. https://doi.org/10.1002/(SICI)1521-4141(199908)29:08<2539::AID-IMMU2539>3.0.CO;2-M PMID:10458769

19. Kosugi A, Sakakura J, Yasuda K, Ogata M, Hamaoka T. Involvement of SHP-1 tyrosine phosphatase in TCR-mediated signaling pathways in lipid rafts. Immunity. 2001; 14:669–80. https://doi.org/10.1016/s1074-7613(01)00146-7 PMID:11420038

20. Binstadt BA, Billadeau DD, Jevremović D, Williams BL, Fang N, Yi T, Koretzky GA, Abraham RT, Leibson PJ. SLP-76 is a direct substrate of SHP-1 recruited to killer cell inhibitory receptors. J Biol Chem. 1998; 273:27518–23. https://doi.org/10.1074/jbc.273.42.27518 PMID:9765283

21. Sharma Y, Ahmad A, Bashir S, Elahi A, Khan F. Implication of protein tyrosine phosphatase SHP-1 in cancer-related signaling pathways. Future Oncol. 2016; 12:1287–98. https://doi.org/10.2217/fon-2015-0057 PMID:26987952

22. Xu E, Schwab M, Marette A. Role of protein tyrosine phosphatases in the modulation of insulin signaling and their implication in the pathogenesis of obesity-linked insulin resistance. Rev Endocr Metab Disord. 2014; 15:79–97. https://doi.org/10.1007/s11154-013-9282-4 PMID:24264858

23. Zhang J, Somani AK, Siminovitch KA. Roles of the SHP-1 tyrosine phosphatase in the negative regulation of cell signalling. Semin Immunol. 2000; 12:361–78. https://doi.org/10.1006/smim.2000.0223 PMID:10995583

24. Xu E, Charbonneau A, Rolland Y, Bellmann K, Pao L, Siminovitch KA, Neel BG, Beauchemin N, Marette A. Hepatocyte-specific Ptpn6 deletion protects from obesity-linked hepatic insulin resistance. Diabetes. 2012; 61:1949–58. https://doi.org/10.2337/db11-1502 PMID:22698917

25. Bergeron S, Dubois MJ, Bellmann K, Schwab M, Larochelle N, Nalbantoglu J, Marette A. Inhibition of the protein tyrosine phosphatase SHP-1 increases glucose uptake in skeletal muscle cells by augmenting insulin receptor signaling and GLUT4 expression. Endocrinology. 2011; 152:4581–8. https://doi.org/10.1210/en.2011-1268 PMID:21952243

26. Dubois MJ, Bergeron S, Kim HJ, Dombrowski L, Perreault M, Fournès B, Faure R, Olivier M, Beauchemin N, Shulman GI, Siminovitch KA, Kim JK, Marette A. The SHP-1 protein tyrosine phosphatase negatively modulates glucose homeostasis. Nat Med. 2006; 12:549–56. https://doi.org/10.1038/nm1397 PMID:16617349

27. Xu E, Forest MP, Schwab M, Avramoglu RK, St-Amand E, Caron AZ, Bellmann K, Shum M, Voisin G, Paquet M, Montoudis A, Lévy E, Siminovitch KA, et al. Hepatocyte-specific Ptpn6 deletion promotes hepatic lipid accretion, but reduces NAFLD in diet-induced obesity: potential role of PPARγ. Hepatology. 2014; 59:1803–15. https://doi.org/10.1002/hep.26957 PMID:24327268

28. Franceschi C, Bonafè M, Valensin S, Olivieri F, De Luca M, Ottaviani E, De Benedictis G. Inflamm-aging. An evolutionary perspective on immunosenescence. Ann N Y Acad Sci. 2000; 908:244–54. https://doi.org/10.1111/j.1749-6632.2000.tb06651.x PMID:10911963

29. Shaw AC, Joshi S, Greenwood H, Panda A, Lord JM. Aging of the innate immune system. Curr Opin Immunol. 2010; 22:507–13. https://doi.org/10.1016/j.coi.2010.05.003 PMID:20667703

30. Guo X, Asthana P, Gurung S, Zhang S, Wong SK, Fallah S, Chow CF, Che S, Zhai L, Wang Z, Ge X, Jiang Z, Wu J, et al. Regulation of age-associated insulin resistance by MT1-MMP-mediated cleavage of insulin receptor. Nat

Commun. 2022; 13:3749.
https://doi.org/10.1038/s41467-022-31563-2
PMID:35768470

31. Carvalho CR, Brenelli SL, Silva AC, Nunes AL, Velloso LA, Saad MJ. Effect of aging on insulin receptor, insulin receptor substrate-1, and phosphatidylinositol 3-kinase in liver and muscle of rats. Endocrinology. 1996; 137:151–9.
https://doi.org/10.1210/endo.137.1.8536607
PMID:8536607

32. Bolinder J, Ostman J, Arner P. Influence of aging on insulin receptor binding and metabolic effects of insulin on human adipose tissue. Diabetes. 1983; 32:959–64.
https://doi.org/10.2337/diab.32.10.959
PMID:6352381

33. Shultz LD, Coman DR, Bailey CL, Beamer WG, Sidman CL. "Viable motheaten," a new allele at the motheaten locus. I. Pathology. Am J Pathol. 1984; 116:179–92.
PMID:6380298

34. Bossé Y, Lamontagne M, Gaudreault N, Racine C, Levesque MH, Smith BM, Auger D, Clemenceau A, Paré MÈ, Laviolette L, Tremblay V, Maranda B, Morissette MC, Maltais F. Early-onset emphysema in a large French-Canadian family: a genetic investigation. Lancet Respir Med. 2019; 7:427–36.
https://doi.org/10.1016/S2213-2600(19)30056-6
PMID:31000475

35. Nesterovitch AB, Szanto S, Gonda A, Bardos T, Kis-Toth K, Adarichev VA, Olasz K, Ghassemi-Najad S, Hoffman MD, Tharp MD, Mikecz K, Glant TT. Spontaneous insertion of a b2 element in the ptpn6 gene drives a systemic autoinflammatory disease in mice resembling neutrophilic dermatosis in humans. Am J Pathol. 2011; 178:1701–14.
https://doi.org/10.1016/j.ajpath.2010.12.053
PMID:21435452

36. Croker BA, Lawson BR, Rutschmann S, Berger M, Eidenschenk C, Blasius AL, Moresco EM, Sovath S, Cengia L, Shultz LD, Theofilopoulos AN, Pettersson S, Beutler BA. Inflammation and autoimmunity caused by a SHP1 mutation depend on IL-1, MyD88, and a microbial trigger. Proc Natl Acad Sci USA. 2008; 105:15028–33.
https://doi.org/10.1073/pnas.0806619105
PMID:18806225

37. Wu L, Zhu X, Liu Y, Zhao D, Yu BC, Wei Z, Lin X, Qi LS. Identification of replicative aging and inflammatory aging signatures via whole-genome CRISPRi screens. Genome Biol. 2025; 26:233.
https://doi.org/10.1186/s13059-025-03683-7
PMID:40770768

38. Wen LZ, Ding K, Wang ZR, Ding CH, Lei SJ, Liu JP, Yin C, Hu PF, Ding J, Chen WS, Zhang X, Xie WF. SHP-1 Acts as a Tumor Suppressor in Hepatocarcinogenesis and HCC Progression. Cancer Res. 2018; 78:4680–91.
https://doi.org/10.1158/0008-5472.CAN-17-3896
PMID:29776962

39. Fan LC, Shiau CW, Tai WT, Hung MH, Chu PY, Hsieh FS, Lin H, Yu HC, Chen KF. SHP-1 is a negative regulator of epithelial-mesenchymal transition in hepatocellular carcinoma. Oncogene. 2015; 34:5252–63.
https://doi.org/10.1038/onc.2014.445 PMID:25619838

40. Becht E, Giraldo NA, Lacroix L, Buttard B, Elarouci N, Petitprez F, Selves J, Laurent-Puig P, Sautès-Fridman C, Fridman WH, de Reyniès A. Estimating the population abundance of tissue-infiltrating immune and stromal cell populations using gene expression. Genome Biol. 2016; 17:218.
https://doi.org/10.1186/s13059-016-1070-5
PMID:27765066

41. Finotello F, Trajanoski Z. Quantifying tumor-infiltrating immune cells from transcriptomics data. Cancer Immunol Immunother. 2018; 67:1031–40.
https://doi.org/10.1007/s00262-018-2150-z
PMID:29541787

42. Aran D, Hu Z, Butte AJ. xCell: digitally portraying the tissue cellular heterogeneity landscape. Genome Biol. 2017; 18:220.
https://doi.org/10.1186/s13059-017-1349-1
PMID:29141660

43. Brandes M, Legler DF, Spoerri B, Schaerli P, Moser B. Activation-dependent modulation of B lymphocyte migration to chemokines. Int Immunol. 2000; 12:1285–92.
https://doi.org/10.1093/intimm/12.9.1285
PMID:10967023

44. Gotoh K, Inoue M, Masaki T, Chiba S, Shimasaki T, Ando H, Fujiwara K, Katsuragi I, Kakuma T, Seike M, Sakata T, Yoshimatsu H. A novel anti-inflammatory role for spleen-derived interleukin-10 in obesity-induced inflammation in white adipose tissue and liver. Diabetes. 2012; 61:1994–2003.
https://doi.org/10.2337/db11-1688 PMID:22648387

45. Wu L, Parekh VV, Hsiao J, Kitamura D, Van Kaer L. Spleen supports a pool of innate-like B cells in white adipose tissue that protects against obesity-associated insulin resistance. Proc Natl Acad Sci USA. 2014; 111:E4638–47.
https://doi.org/10.1073/pnas.1324052111
PMID:25313053

46. Zhao L, Jin S, Wang S, Zhang Z, Wang X, Chen Z, Wang X, Huang S, Zhang D, Wu H. Tertiary lymphoid structures in diseases: immune mechanisms and

therapeutic advances. Signal Transduct Target Ther. 2024; 9:225.
https://doi.org/10.1038/s41392-024-01947-5
PMID:39198425

47. Irvine KM, Skoien R, Bokil NJ, Melino M, Thomas GP, Loo D, Gabrielli B, Hill MM, Sweet MJ, Clouston AD, Powell EE. Senescent human hepatocytes express a unique secretory phenotype and promote macrophage migration. World J Gastroenterol. 2014; 20:17851–62.
https://doi.org/10.3748/wjg.v20.i47.17851
PMID:25548483

48. Sastre J, Pallardó FV, Plá R, Pellín A, Juan G, O'Connor JE, Estrela JM, Miquel J, Viña J. Aging of the liver: age-associated mitochondrial damage in intact hepatocytes. Hepatology. 1996; 24:1199–205.
https://doi.org/10.1002/hep.510240536
PMID:8903398

49. Dasuri K, Zhang L, Ebenezer P, Liu Y, Fernandez-Kim SO, Keller JN. Aging and dietary restriction alter proteasome biogenesis and composition in the brain and liver. Mech Ageing Dev. 2009; 130:777–83.
https://doi.org/10.1016/j.mad.2009.10.003
PMID:19896962

50. Delire B, Lebrun V, Selvais C, Henriet P, Bertrand A, Horsmans Y, Leclercq IA. Aging enhances liver fibrotic response in mice through hampering extracellular matrix remodeling. Aging (Albany NY). 2016; 9:98–113.
https://doi.org/10.18632/aging.101124
PMID:27941216

51. Hilmer SN, Cogger VC, Le Couteur DG. Basal activity of Kupffer cells increases with old age. J Gerontol A Biol Sci Med Sci. 2007; 62:973–8.
https://doi.org/10.1093/gerona/62.9.973
PMID:17895435

52. Wang MJ, Zhang HL, Chen F, Guo XJ, Liu QG, Hou J. The double-edged effects of IL-6 in liver regeneration, aging, inflammation, and diseases. Exp Hematol Oncol. 2024; 13:62.
https://doi.org/10.1186/s40164-024-00527-1
PMID:38890694

53. Baechle JJ, Chen N, Makhijani P, Winer S, Furman D, Winer DA. Chronic inflammation and the hallmarks of aging. Mol Metab. 2023; 74:101755.
https://doi.org/10.1016/j.molmet.2023.101755
PMID:37329949

54. Wahid RM, Hassan NH, Samy W, Abdelhadi AA, Saadawy SF, Elsayed SF, Seada SG, Mohamed SR. Unraveling the hepatic stellate cells mediated mechanisms in aging's influence on liver fibrosis. Sci Rep. 2024; 14:13473.
https://doi.org/10.1038/s41598-024-63644-1
PMID:38866800

55. Novobrantseva TI, Majeau GR, Amatucci A, Kogan S, Brenner I, Casola S, Shlomchik MJ, Koteliansky V, Hochman PS, Ibraghimov A. Attenuated liver fibrosis in the absence of B cells. J Clin Invest. 2005; 115:3072–82.
https://doi.org/10.1172/JCI24798
PMID:16276416

56. Kotsiliti E, Leone V, Schuehle S, Govaere O, Li H, Wolf MJ, Horvatic H, Bierwirth S, Hundertmark J, Inverso D, Zizmare L, Sarusi-Portuguez A, Gupta R, et al. Intestinal B cells license metabolic T-cell activation in NASH microbiota/antigen-independently and contribute to fibrosis by IgA-FcR signalling. J Hepatol. 2023; 79:296–313.
https://doi.org/10.1016/j.jhep.2023.04.037
PMID:37224925

57. Kanemitsu-Okada K, Abe M, Nakamura Y, Miyake T, Watanabe T, Yoshida O, Koizumi Y, Hirooka M, Tokumoto Y, Matsuura B, Koizumi M, Hiasa Y. Role of B Cell-Activating Factor in Fibrosis Progression in a Murine Model of Non-Alcoholic Steatohepatitis. Int J Mol Sci. 2023; 24:2509.
https://doi.org/10.3390/ijms24032509
PMID:36768854

58. Su TH, Shiau CW, Jao P, Yang NJ, Tai WT, Liu CJ, Tseng TC, Yang HC, Liu CH, Huang KW, Hu TC, Huang YJ, Wu YM, et al. Src-homology protein tyrosine phosphatase-1 agonist, SC-43, reduces liver fibrosis. Sci Rep. 2017; 7:1728.
https://doi.org/10.1038/s41598-017-01572-z
PMID:28496142

59. Zhao YL, Zhu RT, Sun YL. Epithelial-mesenchymal transition in liver fibrosis. Biomed Rep. 2016; 4:269–74.
https://doi.org/10.3892/br.2016.578 PMID:26998262

60. Yu K, Li Q, Shi G, Li N. Involvement of epithelial-mesenchymal transition in liver fibrosis. Saudi J Gastroenterol. 2018; 24:5–11.
https://doi.org/10.4103/sjg.SJG_297_17
PMID:29451178

61. Wang H, Lafdil F, Wang L, Park O, Yin S, Niu J, Miller AM, Sun Z, Gao B. Hepatoprotective versus oncogenic functions of STAT3 in liver tumorigenesis. Am J Pathol. 2011; 179:714–24.
https://doi.org/10.1016/j.ajpath.2011.05.005
PMID:21684247

62. Winer DA, Winer S, Shen L, Wadia PP, Yantha J, Paltser G, Tsui H, Wu P, Davidson MG, Alonso MN, Leong HX, Glassford A, Caimol M, et al. B cells promote insulin resistance through modulation of T cells and production of pathogenic IgG antibodies. Nat Med. 2011; 17:610–7.
https://doi.org/10.1038/nm.2353 PMID:21499269

63. Carter S, Miard S, Caron A, Sallé-Lefort S, St-Pierre P, Anhê FF, Lavoie-Charland E, Blais-Lecours P, Drolet MC, Lefebvre JS, Lacombe J, Deshaies Y, Couet J, et al. Loss of OcaB Prevents Age-Induced Fat Accretion and Insulin Resistance by Altering B-Lymphocyte Transition and Promoting Energy Expenditure. Diabetes. 2018; 67:1285–96. https://doi.org/10.2337/db17-0558 PMID:29496744

64. Shen L, Chng MH, Alonso MN, Yuan R, Winer DA, Engleman EG. B-1a lymphocytes attenuate insulin resistance. Diabetes. 2015; 64:593–603. https://doi.org/10.2337/db14-0554 PMID:25249575

65. Harmon DB, Srikakulapu P, Kaplan JL, Oldham SN, McSkimming C, Garmey JC, Perry HM, Kirby JL, Prohaska TA, Gonen A, Hallowell P, Schirmer B, Tsimikas S, et al. Protective Role for B-1b B Cells and IgM in Obesity-Associated Inflammation, Glucose Intolerance, and Insulin Resistance. Arterioscler Thromb Vasc Biol. 2016; 36:682–91. https://doi.org/10.1161/ATVBAHA.116.307166 PMID:26868208

66. Nishimura S, Manabe I, Takaki S, Nagasaki M, Otsu M, Yamashita H, Sugita J, Yoshimura K, Eto K, Komuro I, Kadowaki T, Nagai R. Adipose Natural Regulatory B Cells Negatively Control Adipose Tissue Inflammation. Cell Metab. 2013; 18:759–66. https://doi.org/10.1016/j.cmet.2013.09.017 PMID:24209772

67. Miura A, Hosono T, Seki T. Macrophage potentiates the recovery of liver zonation and metabolic function after acute liver injury. Sci Rep. 2021; 11:9730. https://doi.org/10.1038/s41598-021-88989-9 PMID:33958644

68. Park MH, Kim DH, Lee EK, Kim ND, Im DS, Lee J, Yu BP, Chung HY. Age-related inflammation and insulin resistance: a review of their intricate interdependency. Arch Pharm Res. 2014; 37:1507–14. https://doi.org/10.1007/s12272-014-0474-6 PMID:25239110

69. Pao LI, Lam KP, Henderson JM, Kutok JL, Alimzhanov M, Nitschke L, Thomas ML, Neel BG, Rajewsky K. B cell-specific deletion of protein-tyrosine phosphatase Shp1 promotes B-1a cell development and causes systemic autoimmunity. Immunity. 2007; 27:35–48. https://doi.org/10.1016/j.immuni.2007.04.016 PMID:17600736

70. Myers DR, Abram CL, Wildes D, Belwafa A, Welsh AM, Schulze CJ, Choy TJ, Nguyen T, Omaque N, Hu Y, Singh M, Hansen R, Goldsmith MA, et al. Shp1 Loss Enhances Macrophage Effector Function and Promotes Anti-Tumor Immunity. Front Immunol. 2020; 11:576310. https://doi.org/10.3389/fimmu.2020.576310 PMID:33133093

71. Moussavi-Harami SF, Cleary SJ, Magnen M, Seo Y, Conrad C, English BC, Qiu L, Wang KM, Abram CL, Lowell CA, Looney MR. Neutrophil-specific Shp1 loss results in lethal pulmonary hemorrhage in mouse models of acute lung injury. J Clin Invest. 2024; 134:e183161. https://doi.org/10.1172/JCI183161 PMID:39352872

72. Foster CJ, Du J, Pundel O, Geer MJ, Ripert RC, Liu J, Heim TA, Araki KY, Lund AW, Wang J, Neel BG. T lymphocyte-specific deletion of SHP1 and SHP2 promotes activation-induced cell death of $CD4^+$ T cells and impairs antitumor response. Proc Natl Acad Sci USA. 2025; 122:e2427254122. https://doi.org/10.1073/pnas.2427254122 PMID:40658856

73. Shultz LD, Rajan TV, Greiner DL. Severe defects in immunity and hematopoiesis caused by SHP-1 protein-tyrosine-phosphatase deficiency. Trends Biotechnol. 1997; 15:302–7. https://doi.org/10.1016/S0167-7799(97)01060-3 PMID:9263478

74. Pineault M, Milad N, Bouffard G, Tremblay F, Routhier J, Beaulieu MJ, Aubin S, Lechasseur A, Bossé Y, Maltais F, Morissette MC. A mutation in PTPN6 associated to emphysema alters B-lymphocyte biology in humans and mice. J Immunol. 2026;215:vkag162. https://doi.org/10.1093/jimmun/vkag162 PMID:42426938

75. Folch J, Lees M, Sloane Stanley GH. A simple method for the isolation and purification of total lipides from animal tissues. J Biol Chem. 1957; 226:497–509. PMID:13428781

76. Izzi L, Turbide C, Houde C, Kunath T, Beauchemin N. cis-Determinants in the cytoplasmic domain of CEACAM1 responsible for its tumor inhibitory function. Oncogene. 1999; 18:5563–72. https://doi.org/10.1038/sj.onc.1202935 PMID:10523833

77. Seglen PO. Preparation of isolated rat liver cells. Methods Cell Biol. 1976; 13:29–83. https://doi.org/10.1016/s0091-679x(08)61797-5 PMID:177845

78. Andrews S. Fastqc: a quality control tool for high throughput sequence data. https://www.bioinformatics.babraham.ac.uk/projects/fastqc/. 2010.

79. Krueger F. Trim galore. https://github.com/FelixKrueger/TrimGalore. 2021.

80. Bray NL, Pimentel H, Melsted P, Pachter L. Near-optimal probabilistic RNA-seq quantification. Nat Biotechnol. 2016; 34:525–7.

https://doi.org/10.1038/nbt.3519 PMID:27043002

81. Soneson C, Love MI, Robinson MD. Differential analyses for RNA-seq: transcript-level estimates improve gene-level inferences. F1000Res. 2015; 4:1521. https://doi.org/10.12688/f1000research.7563.2 PMID:26925227

82. Love MI, Huber W, Anders S. Moderated estimation of fold change and dispersion for RNA-seq data with DESeq2. Genome Biol. 2014; 15:550. https://doi.org/10.1186/s13059-014-0550-8 PMID:25516281

83. Liberzon A, Subramanian A, Pinchback R, Thorvaldsdóttir H, Tamayo P, Mesirov JP. Molecular signatures database (MSigDB) 3.0. Bioinformatics. 2011; 27:1739–40. https://doi.org/10.1093/bioinformatics/btr260 PMID:21546393

84. Castanza AS, Recla JM, Eby D, Thorvaldsdóttir H, Bult CJ, Mesirov JP. Extending support for mouse data in the Molecular Signatures Database (MSigDB). Nat Methods. 2023; 20:1619–20. https://doi.org/10.1038/s41592-023-02014-7 PMID:37704782

85. Hänzelmann S, Castelo R, Guinney J. GSVA: gene set variation analysis for microarray and RNA-seq data. BMC Bioinformatics. 2013; 14:7. https://doi.org/10.1186/1471-2105-14-7 PMID:23323831

86. Petitprez F, Levy S, Sun CM, Meylan M, Linhard C, Becht E, Elarouci N, Tavel D, Roumenina LT, Ayadi M, Sautès-Fridman C, Fridman WH, de Reyniès A. The murine Microenvironment Cell Population counter method to estimate abundance of tissue-infiltrating immune and stromal cell populations in murine samples using gene expression. Genome Med. 2020; 12:86. https://doi.org/10.1186/s13073-020-00783-w PMID:33023656

87. Durinck S, Moreau Y, Kasprzyk A, Davis S, De Moor B, Brazma A, Huber W. BioMart and Bioconductor: a powerful link between biological databases and microarray data analysis. Bioinformatics. 2005; 21:3439–40. https://doi.org/10.1093/bioinformatics/bti525 PMID:16082012

88. Durinck S, Spellman PT, Birney E, Huber W. Mapping identifiers for the integration of genomic datasets with the R/Bioconductor package biomaRt. Nat Protoc. 2009; 4:1184–91. https://doi.org/10.1038/nprot.2009.97 PMID:19617889

89. Liang W, Menke AL, Driessen A, Koek GH, Lindeman JH, Stoop R, Havekes LM, Kleemann R, van den Hoek AM. Establishment of a general NAFLD scoring system for rodent models and comparison to human liver pathology. PLoS One. 2014; 9:e115922. https://doi.org/10.1371/journal.pone.0115922 PMID:25535951

90. Edgar R, Domrachev M, Lash AE. Gene Expression Omnibus: NCBI gene expression and hybridization array data repository. Nucleic Acids Res. 2002; 30:207–10. https://doi.org/10.1093/nar/30.1.207 PMID:11752295

SUPPLEMENTARY MATERIALS

Supplementary Figures

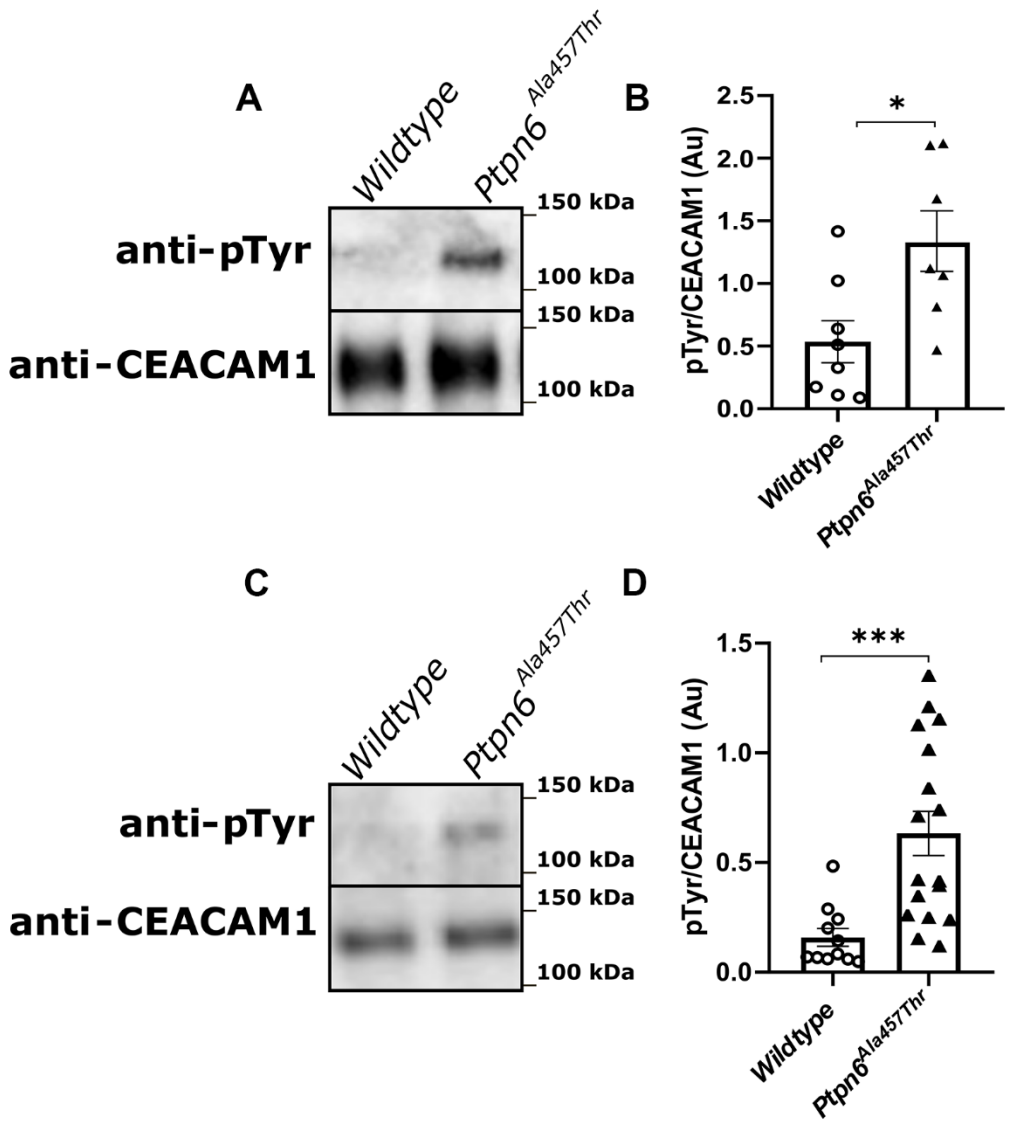

Supplementary Figure 1. Tyrosine phosphorylation of CEACAM1 is increased in *Ptpn6*^{Ala457Thr} mutants. (**A**) Representative western blot showing immunoprecipitated CEACAM1 protein and its tyrosine phosphorylation levels in liver tissue from young adult wildtype (WT) and *Ptpn6*^{Ala457Thr} mice detected with CEACAM1 and pTyr-specific (Mix of PY20/4G10) antibodies. (**B**) Quantification of CEACAM1 tyrosine phosphorylation levels in young adult mice from panel a. (**C**) Representative western blot showing immunoprecipitated CEACAM1 protein and its tyrosine phosphorylation levels in liver tissue from old WT and *Ptpn6*^{Ala457Thr} mice detected as in a. (**D**) Quantification of CEACAM1 tyrosine phosphorylation levels in old mice from panel c. Data are presented as mean ± SEM. Statistical significance was determined by unpaired two-tailed Student's *t*-test, with *$p < 0.05$, ***$p < 0.001$. Sample sizes: young adult wildtype, n=8; *Ptpn6*^{Ala457Thr}, n = 7 and old wildtype, n = 11; *Ptpn6*^{Ala457Thr}, n=18. Au, arbitrary units.

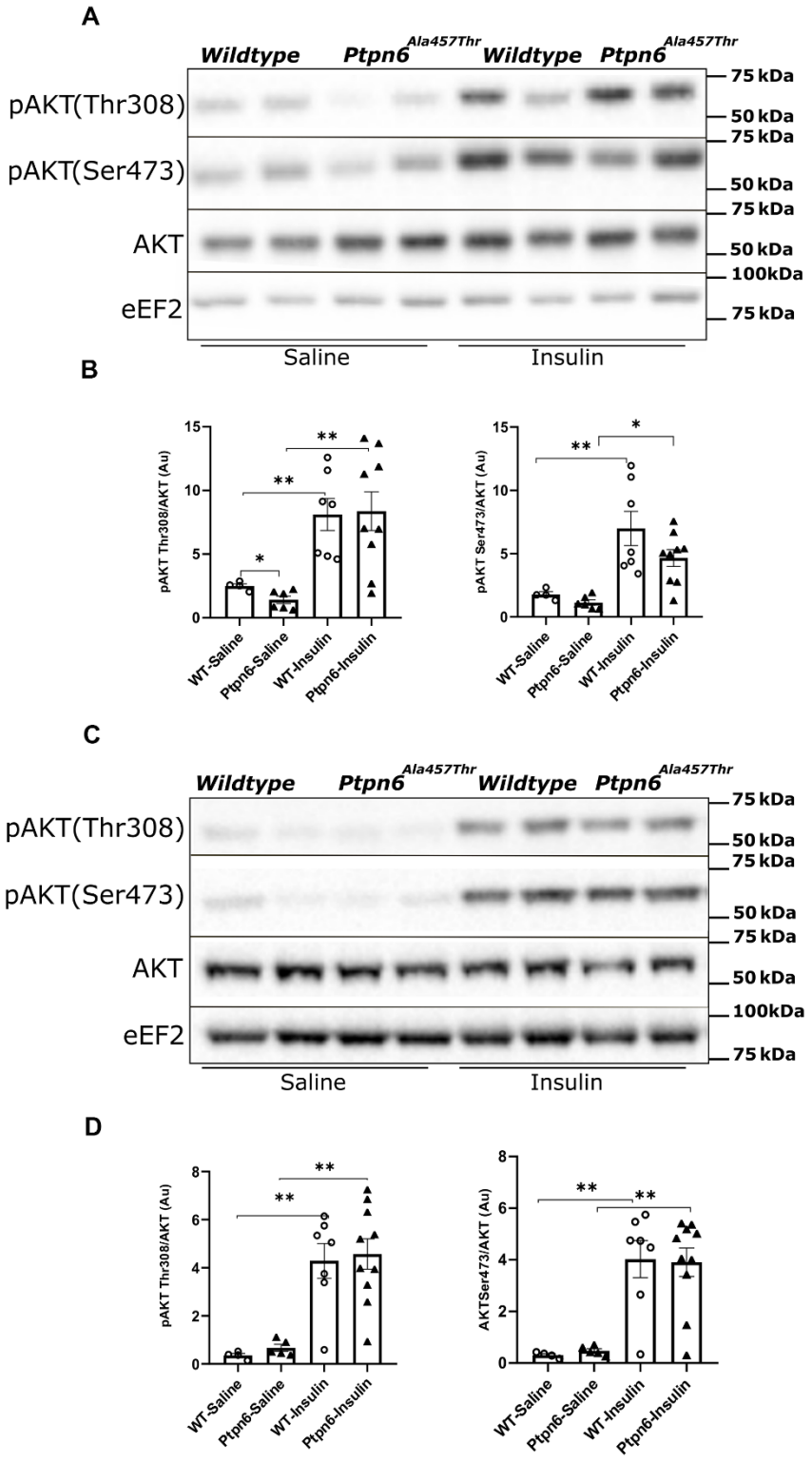

Supplementary Figure 2. AKT phosphorylation is not altered in adipose tissue or skeletal muscle of aged *Ptpn6*^{Ala457Thr} mice. (**A**) Western blot analysis of AKT phosphorylation in mesenteric white adipose tissue (mWAT). (**B**) Quantification of phospho-AKT (Thr308) and phospho-AKT (Ser473) levels normalized to total AKT from panel (**A**). (**C**) Western blot analysis of AKT phosphorylation in gastrocnemius muscle (Gastroc). (**D**) Quantification of phospho-AKT (Thr308) and phospho-AKT (Ser473) levels normalized to total AKT from panel (**C**). Data are presented as mean ± SEM. Statistical analysis was performed using two-way ANOVA followed by Tukey's post hoc test, with *$p < 0.05$, **$p < 0.01$. Sample sizes: WT, n = 11; *Ptpn6*^{Ala457Thr}, n = 15. Au, arbitrary units.

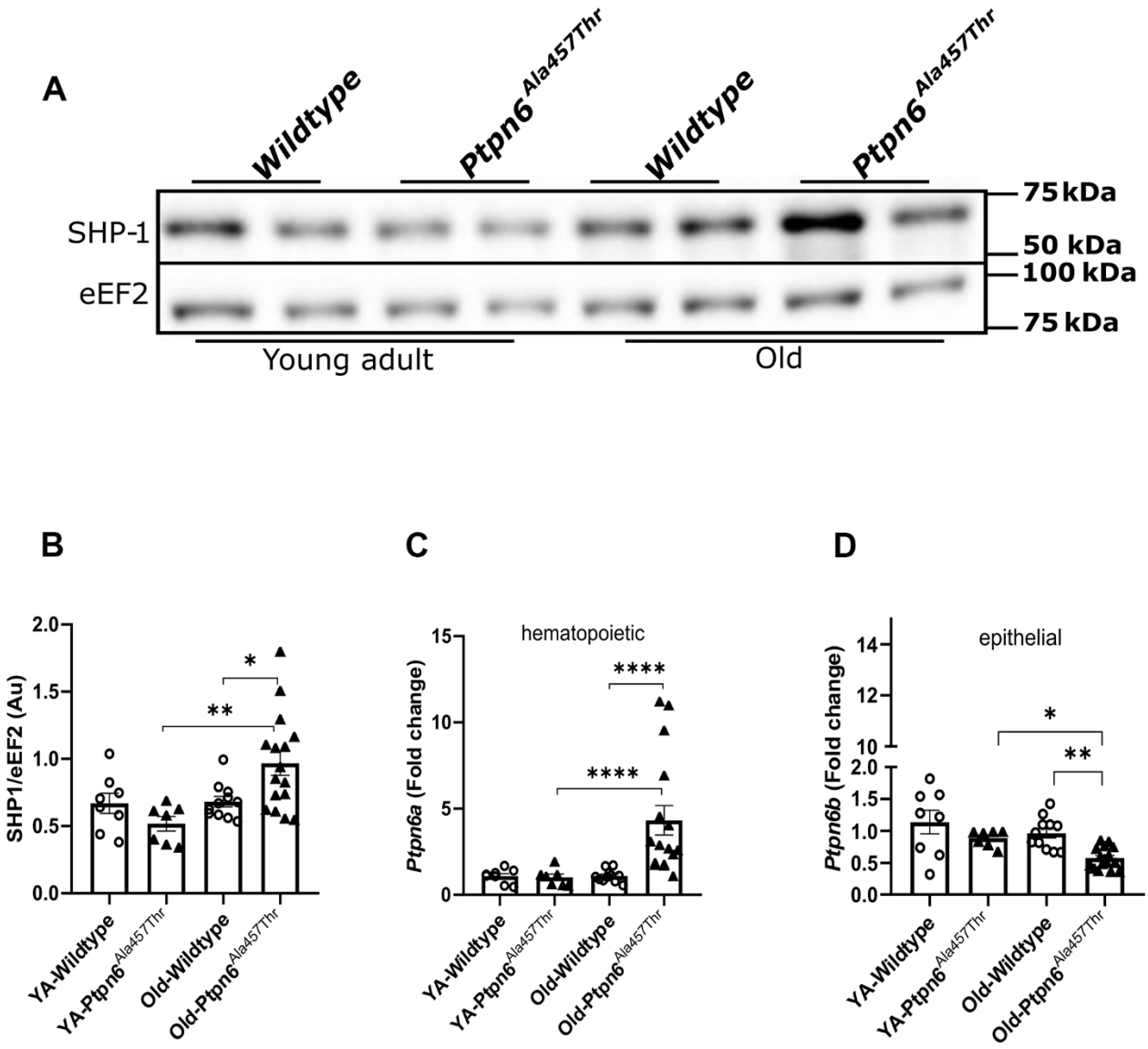

Supplementary Figure 3. SHP-1 levels track immune load in the liver. (**A**) Representative western blot analyses of SHP-1 protein expression in liver lysates from young adult and old wildtype and *Ptpn6*^{Ala457Thr} mice. (**B**) Quantification of SHP-1 levels from (**A**). (**C**) Gene expression of hematopoietic *Ptpn6a* and (**D**) epithelial *Ptpn6b* isoforms respectively in liver transcripts from young adult and old WT and *Ptpn6*^{Ala457Thr} mice. Data are represented as mean ± SEM. Statistical significance was determined using two-way ANOVA followed by Tukey's post hoc test, with *p < 0.05, **p < 0.01, ***p < 0.001. Sample sizes: Young adult (YA) WT, n=8; *Ptpn6*^{Ala457Thr}, n=7 and old WT, n=11; *Ptpn6*^{Ala457Thr}, n=16. Au, arbitrary units.

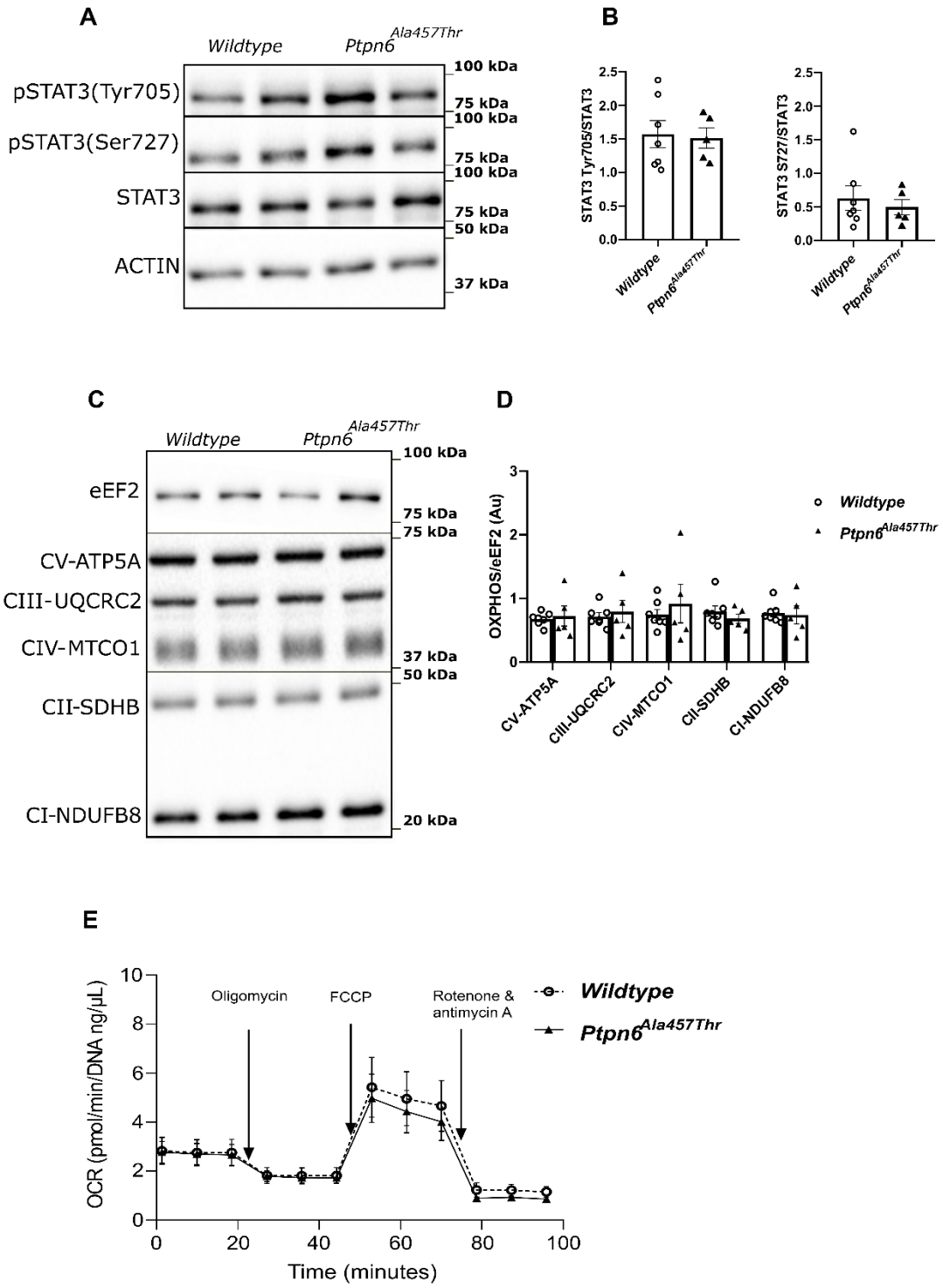

Supplementary Figure 4. *Ptpn6*^{Ala457Thr} mutation does not alter STAT3 phosphorylation or mitochondrial function in primary mouse hepatocytes. (**A**) Western blot analyses of phosphorylated STAT3 (Tyr705), phosphorylated STAT3 (Ser727) and total STAT3 in primary mouse hepatocytes from old wildtype and *Ptpn6*^{Ala457Thr} mice. (**B**) Quantification of phospho-STAT3 (Tyr705), phospho-STAT3 (Ser727), normalized to total STAT3. (**C**) Western blot analyses showing expression of the oxidative phosphorylation protein complex (OXPHOS) (Complexes I–V). (**D**) Quantification of OXPHOS complex proteins from (**C**). (**E**) Oxygen consumption rate (OCR) measured in primary hepatocytes using the Seahorse XF Analyzer (samples size: WT, n=8; *Ptpn6*^{Ala457Thr}, n=6). Data are represented as mean ± SEM. Statistical significance was determined using Unpaired two-tailed Student's t test and a two-way ANOVA followed by Tukey's post hoc test with *$p < 0.05$, **$p < 0.01$, ***$p < 0.001$. Sample sizes WT, n=6; *Ptpn6*^{Ala457Thr}, n=5. Au, arbitrary units.

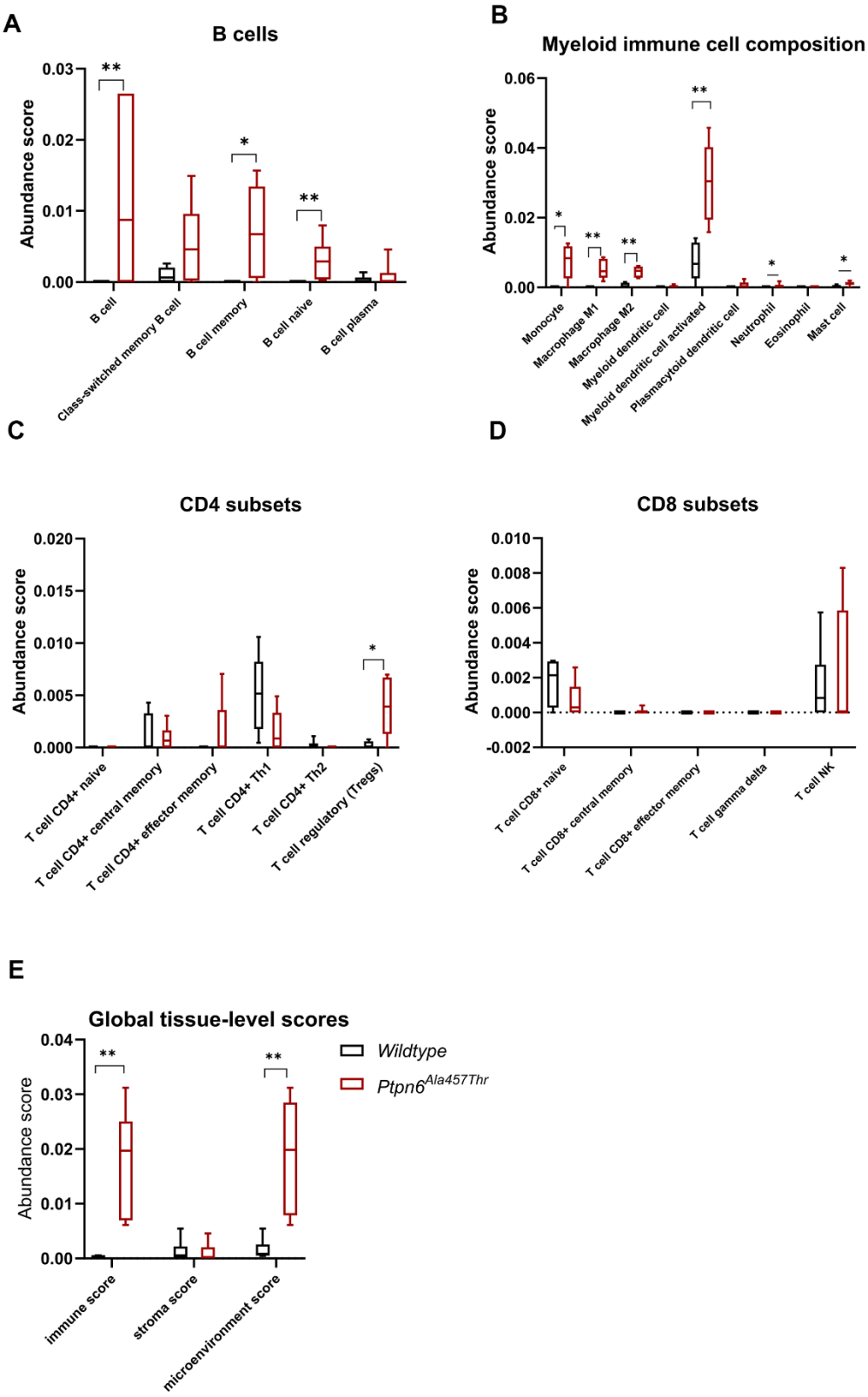

Supplementary Figure 5. RNA-seq-based immune cell deconvolution of liver tissue. (**A**) B cells. (**B**) Myeloid immune cell composition. (**C**) CD4 T cell subsets. (**D**) CD8 T cell subsets. (**E**) Global tissue-level scores. Data are represented as mean ± SEM. Statistical significance was determined using unpaired two-tailed Student's t test with *$p < 0.05$, **p < 0.01, ***$p < 0.001$. Sample sizes n=6.

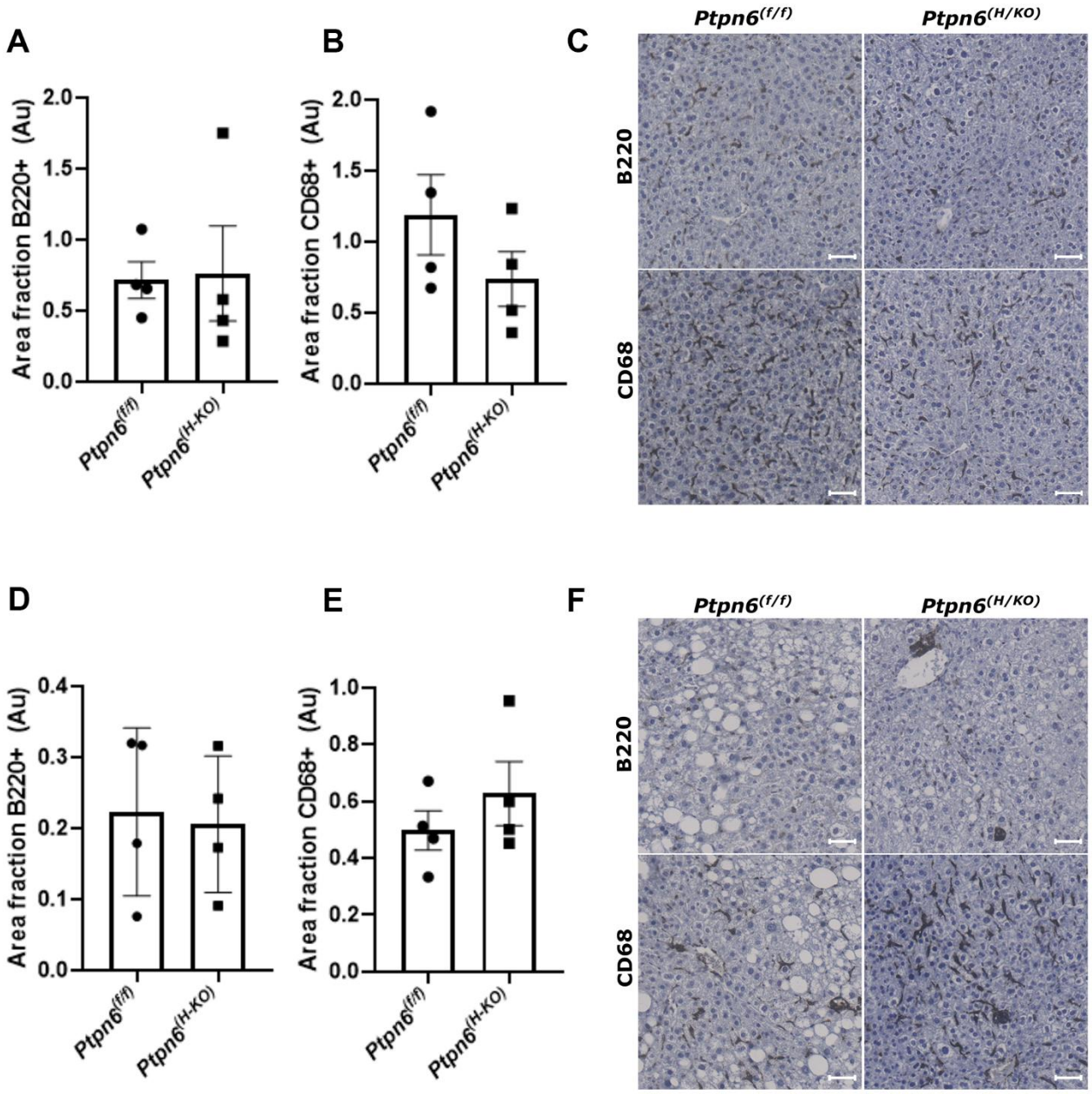

Supplementary Figure 6. B220 and CD68 expression in the liver of old *Ptpn6*$^{(fl/fl)}$ and *Ptpn6*$^{(H\text{-}KO)}$ female and male mice. (**A**) Area fraction of B220-positive staining in liver sections from female mice. (**B**) Area fraction of CD68-positive staining in liver sections from female mice. (**C**) Representative immunohistochemistry images of liver sections stained for B220 (B cells) and CD68 (macrophages) in control *Ptpn6*$^{(fl/fl)}$ and *Ptpn6*$^{(H\text{-}KO)}$ female mice. (**D**) Area fraction of B220-positive staining in liver sections from male mice. (**E**) Area fraction of CD68-positive staining in liver sections from male mice. (**F**) Representative immunohistochemistry images of liver sections stained for B220 (B cells) and CD68 (macrophages) in control *Ptpn6*$^{(H\text{-}KO)}$ and *Ptpn6*$^{(H\text{-}KO)}$ old male mice. Data are presented as mean ± SEM. Statistical analysis was performed using unpaired two-tailed Student's t-test with *p < 0.05, **p < 0.01, ***p < 0.001. Sample sizes: Females: *Ptpn6*$^{(fl/fl)}$, n=4; *Ptpn6*$^{(H\text{-}KO)}$, n=4; males: *Ptpn6*$^{(fl/fl)}$, n=4; *Ptpn6*$^{(H\text{-}KO)}$, n=4. Scale bar: 50 µm.

Supplementary Table

Supplementary Table 1. Relative tissue weights of old *wildtype* and *Ptpn6*^{Ala457Thr} mice.

Tissue (% of BW)	*Wildtype* (Mean ±SEM)	*Ptpn6*^{Ala457Thr} (Mean±SEM)	p-value
Liver	3,86±0,095	3,77±0,08	0,5801
mWAT	1,71±0,08	1,32±0,09	**0,007**
BAT	0,42±0,03	0,3±0,02	**0,0144**
Kidneys	0,99±0,048	1,05±0,036	0,1881
Soleus	0,038±0,002	0,039±0,001	0,912
Gastroc	0,58±0,02	0,66±0,01	**0,0442**
iWAT	2,53±0,28	1,85±0,23	0,0682
Spleen	0,16±0,008	1,08±0,17	**<0,0001**

Tissue weights relative to body mass are expressed as a percentage (%) of body weight. Statistical analyses were performed using an unpaired Student's t-test. Significant p-values are shown in bold.